RESEARCH ARTICLE

Key Points:
- Automated data-filtering protocol improves clarity and reduces uncertainty of magnetostratigraphies measured in weakly magnetized sediments
- Magnetostratigraphy dates this interval of Site U1406 to ~21–27 Ma and includes new normal polarity events in Chrons C6Br, C7r, and C7Ar
- Behavior of sediment drifts in the northwest Atlantic Ocean is linked to global cold periods and the strength of deep-water currents

Supporting Information:
- Supporting Information S1
- Table S1
- Table S2
- Table S3
- Table S4

Correspondence to:
T. E. van Peer,
T.E.vanPeer@soton.ac.uk

Extracting a Detailed Magnetostratigraphy From Weakly Magnetized, Oligocene to Early Miocene Sediment Drifts Recovered at IODP Site U1406 (Newfoundland Margin, Northwest Atlantic Ocean)

Tim E. van Peer[1] (iD), **Chuang Xuan**[1] (iD), **Peter C. Lippert**[2] (iD), **Diederik Liebrand**[1] (iD), **Claudia Agnini**[3,4] (iD), and **Paul A. Wilson**[1] (iD)

[1]National Oceanography Centre Southampton, University of Southampton Waterfront Campus, Southampton, UK, [2]Department of Geology and Geophysics, University of Utah, Salt Lake City, UT, USA, [3]Department of Geosciences, University of Padova, Padova, Italy, [4]Department of Geological Sciences, Stockholm University, Stockholm, Sweden

Abstract Fine-grained magnetic particles in deep-sea sediments often statistically align with the ambient magnetic field during (and shortly after) deposition and can therefore record geomagnetic reversals. Correlation of these reversals to a geomagnetic polarity time scale is an important geochronological tool that facilitates precise stratigraphic correlation and dating of geological records globally. Sediments often carry a remanence strong enough for confident identification of polarity reversals, but in some cases a low signal-to-noise ratio prevents the construction of a reliable and robust magnetostratigraphy. Here we implement a data-filtering protocol, which can be integrated with the UPmag software package, to automatically reduce the maximum angular deviation and statistically mask noisy data and outliers deemed unsuitable for magnetostratigraphic interpretation. This protocol thus extracts a clearer signal from weakly magnetized sediments recovered at Integrated Ocean Drilling Program (IODP) Expedition 342 Site U1406 (Newfoundland margin, northwest Atlantic Ocean). The resulting magnetostratigraphy, in combination with shipboard and shore-based biostratigraphy, provides an age model for the study interval from IODP Site U1406 between Chrons C6Ar and C9n (~21–27 Ma). We identify rarely observed geomagnetic directional changes within Chrons C6Br, C7r, and C7Ar, and perhaps within Subchron C8n.1n. Our magnetostratigraphy dates three intervals of unusual stratigraphic behavior within the sediment drifts at IODP Site U1406 on the Newfoundland margin. These lithostratigraphic changes are broadly concurrent with the coldest climatic phases of the middle Oligocene to early Miocene and we hypothesize that they reflect changes in bottom water circulation.

1. Introduction

Since the 1960s, the geomagnetic polarity time scale (GPTS) has become established as a widely applied tool for the development of accurate age models and global stratigraphic correlations. Magnetic reversals observed in marine magnetic anomaly profiles were initially supported and subsequently improved by the construction of magnetostratigraphies from continuous sedimentary sequences recovered during deep-sea drilling. Today most of the geomagnetic field reversals of the Cenozoic era are well dated using astronomical tuning and radiometric dating methods (e.g., Hilgen et al., 2012; Vandenberghe et al., 2012) and therefore provide high-fidelity age control for important geological events. For example, the six reversals within Chron C6Cn (nomenclature cf., Cande & Kent, 1992) occur contemporaneously with the Oligocene-Miocene Transition (OMT) climate event. The precision of the magnetostratigraphic age control is independent from climate proxy records and therefore key to global correlations required for a more complete understanding of the causes and consequences of this climate event.

One major obstacle to develop reliable magnetostratigraphic chronologies of these important geological events is the occurrence of very low natural remanent magnetization (NRM) intensities that is sometimes present in deep-sea sequences. This low intensity can be a primary effect caused by low ferromagnetic mineral supply, result from dilution by nonremanence phases (e.g., Roberts et al., 2013), be authigenic or diagenetic (e.g., Roberts, 2015), or a combination of these. A good example of this problem arises in the
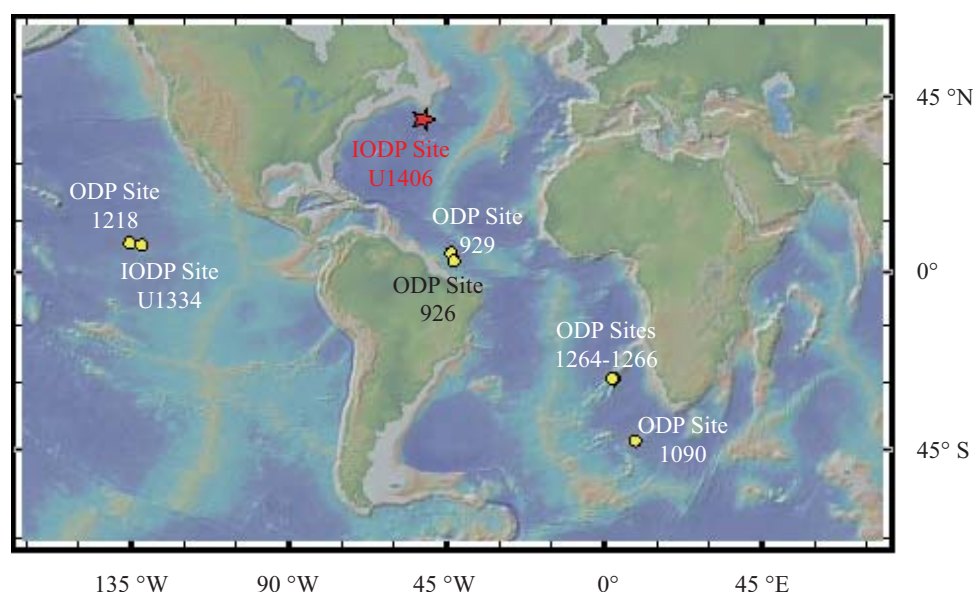
Figure 1. Location of Integrated Ocean Drilling Program (IODP) Expedition 342 Site U1406 highlighted with a red star on present-day bathymetry map (prepared using www.geomapapp.org). Yellow dots indicate other IODP and Ocean Drilling Program (ODP) sites with well-established Oligocene to Miocene magnetostratigraphies or climate records including ODP Sites 926 and 929 (Pälike et al., 2006a), ODP Site 1090 (Billups et al., 2004; Channell et al., 2003), ODP Site 1218 (Lanci et al., 2005; Pälike et al., 2006b), ODP Sites 1264 through 1266 (Liebrand et al., 2016, 2017), and IODP Site U1334 (Channell et al., 2013).

Oligocene to Miocene sediment drift deposits of the Newfoundland margin recovered from Integrated Ocean Drilling Program (IODP) Expedition 342 Site U1406, where the NRM intensity measured shipboard is in the range $\sim10^{-4}$ to $\sim10^{-5}$ A/m after 20 mT peak alternating field demagnetization (Norris et al., 2014). This weak magnetization, together with lower measurement sensitivity and incomplete shipboard demagnetization protocols, precluded the construction of a full and rigorous magnetostratigraphy in certain intervals, most notably around the OMT.

Here we implement a multistep paleomagnetic data analysis protocol that improves the identification, analysis, and interpretation of magnetozones in weakly magnetized samples after a complete sequence of shore-based demagnetization. The protocol objectively selects the highest quality NRM data for magnetostratigraphic interpretation. The shore-based measurements and application of this protocol make it possible to substantially enhance the signal-to-noise ratio of the NRM measurements in comparison to the shipboard data. We fully demagnetized and measured 159 u-channel samples (typically 1.5 m long, with a $\sim2 \times 2$ cm^2 cross section, Tauxe et al., 1983) at IODP Site U1406 and adopt the new composite depth scale and splice (van Peer et al., 2017) that removes ambiguities in the shipboard depth scale. The resulting magnetostratigraphy allows us to identify rarely observed polarity changes (e.g., Channell et al., 2003, 2013; Lanci et al., 2005) and firmly places IODP Site U1406 in a global chronostratigraphic framework of middle Oligocene to early Miocene climate and oceanographic records.

2. Samples and Methods

2.1. Site Description

IODP Site U1406 is located near the crest of the J-Anomaly Ridge, on the Newfoundland margin in the northwest Atlantic Ocean (Figure 1). The site is at intermediate paleodepths within the Expedition 342-wide depth transect that aims to document changes in the North Atlantic carbonate compensation depth. The Eocene-Miocene interval at IODP Site U1406 consists of clay-rich nannofossil oozes and chalks (Norris et al., 2014). The sediments are light greenish to grey in color and are well bioturbated with occasional glauconitic horizons (Norris et al., 2014) that suggest prolonged exposure on the sea floor. For example, an exceptionally well-developed, ~10 cm-thick glauconite horizon (Figure 2a) occurs at ~34.5 m CCSF-M (Core Composite depth below Sea Floor, where Method "M" denotes that off-splice intervals are mapped to the splice, cf.,

a) Image
Glauconite

b) Image
Slump

Figure 2. Core section photos (Norris et al., 2014) in (a and b) are highlighting the strongly developed glauconitic horizon and slumped interval, respectively

van Peer et al., 2017). Additionally, interhole variability is present at ~94 m CCSF-M, which consists of a condensed interval in Hole U1406A, a ~2 m hiatus in Hole U1406B between 93 and 95 m CCSF-M, and an apparent stratigraphically complete record in Hole U1406C (van Peer et al., 2017). Furthermore, contorted bedding and microfaults (Figure 2b) appear at ~175 m CCSF-M, which has been interpreted as slumping (Norris et al., 2014).

2.2. Samples and Magnetic Measurements

A total of 159 u-channel samples were taken from the center of archive-half core sections at IODP Site U1406 to avoid sampling of the sheared core-margins that could degrade paleomagnetic measurements (e.g., Acton et al., 2002). Sampling followed the shipboard splice (Norris et al., 2014) and we accounted for stratigraphic complexities and splice revisions (van Peer et al., 2017) by collecting additional off-splice u-channel samples. Working-half core sections were sampled where archive-half core sections were designated as a permanent archive. The NRM of all u-channel samples was measured on a 2G Enterprises Model-760R superconducting rock magnetometer housed in a magnetically shielded room at the National Oceanography Centre Southampton, University of Southampton (UoS), UK. This system was designed for measurement of u-channel samples and has a narrow-bore sample access hole (Weeks et al., 1993), which introduces less convolution (smoothing) during pass-through measurements. We measured the NRM of all u-channel samples repeatedly at 1 cm intervals before and after stepwise alternating field (AF) demagnetization at peak fields of 20–60 mT in 5 mT increments, and at 80 and 100 mT (12 steps in total).

We also collected 21 bulk sediment samples from selected depth levels for room temperature rock magnetic experiments. Each sample weighed ~1 g and was encapsulated and immobilized with sodium silicate. After consolidation, we measured hysteresis loops and backfield curves of the samples to estimate hysteresis parameters (i.e., M_s saturation magnetization, M_r saturation remanence, H_{cr} coercivity of remanence, and H_c coercivity). Measurements were carried out on a Princeton Measurements Corporation (now Lake Shore Cryotronics) Model 3900-02 vibrating sample magnetometer (VSM) at UoS, using a 10 s averaging time, 5 mT field-step increments, and a saturating field of 500 mT for both hysteresis loops and backfield curves. We used the Institute for Rock Magnetism Database software (Jackson & Solheid, 2010) to process the measured hysteresis loops.

Fifteen bulk samples were selected for First-Order Reversal Curve (FORC) measurements (Pike et al., 1999; Roberts et al., 2000, 2014) on a VSM at UoS. FORC diagrams consisted of 80 curves at ~3.5 mT field increments and were analyzed using the FORCinel v. 2.03 software (Harrison & Feinberg, 2008), which incorporates VARIFORC smoothing (Egli, 2013) and statistical confidence intervals (Heslop & Roberts, 2012). All FORC diagrams were mass normalized and drift corrected, with the first point artifact removed and five lower branches subtracted to enhance the FORC signal (Egli, 2013). The generally weak magnetization of the samples required high VARIFORC smoothing factors (i.e., $S_{c,0} = 5$–7; $S_{c,1} = 5$–8), in addition to a ~14 h measurement protocol with a 10 s averaging time.

Magnetic susceptibility of eleven freeze-dried bulk sediment samples was measured either during warming from room temperature (RT) to 600°C followed by cooling to RT in a 200 A/m AC field, on an AGICO multi-function Kappabridge with a CS4 furnace at the Institute for Rock Magnetism (University of Minnesota), or from RT to 700°C followed by cooling to RT in a 300 A/m AC field on an AGICO KLY-4S with a CS3 furnace at UoS. The latter experiments were carried out to test for possible alteration at temperatures >600°C. All samples were heated at ~11°C/min in an argon atmosphere to minimize potential alteration during heating.

2.3. NRM Data Processing and Noise-Masking Protocol

Measurements of the relatively weak NRM (intensity ~10^{-5} to 10^{-4} A/m after 20 mT peak AF demagnetization) of IODP Site U1406 sediments were prone to noise. Principal component analyses (PCA) (Kirschvink,

1980) of the u-channel NRM data, using a commonly applied, uniform demagnetization range (i.e., 20–60 mT; e.g., Channell et al., 2013), frequently resulted in maximum angular deviation (MAD) values >15°, indicating poorly defined component directions. Recognizing the limitations of applying a uniform demagnetization range for direction assignments, we investigated the application of a set of data selection criteria that automatically masks statistical outliers or measurements significantly affected by environmental or instrument noise, leaving better-resolved data for magnetostratigraphic interpretations. Despite several similarities, our analytical procedure was developed independently from the Zplotit software (Acton, 2011) and was designed specifically for integration with the UPmag software suite (Xuan & Channell, 2009).

For NRM data of each 1 cm interval, we first calculated PCA directions for all possible six-step combinations from 10 steps in the 20–80 mT range. We did not anchor the origin to avoid introducing artificially low uncertainty estimates (Heslop & Roberts, 2016). Only PCA directions associated with the six-step combination yielding the minimum MAD value were used for further interpretation. This procedure automatically discards data from noisy measurement steps, which improved the rigor of the resulting PCA directions. In addition, we calculated Fisher's statistics using the data from the six demagnetization steps that produce the optimal PCA directions. The associated α_{95} values (error estimate of Fisher's mean) provided an additional check on the measurement data quality. For example, demagnetization data that lied closely on a line in orthogonal vector space would have yielded a small MAD value, but the defined line may not cross near the origin. Such data would be associated with large α_{95} values.

To construct the magnetostratigraphy at IODP Site U1406 using only the highest quality NRM data, we removed data from (1) disturbed intervals (e.g., coring-induced or sampling-induced) described during shipboard operations (Norris et al., 2014) and after visual inspection of core-images and u-channel samples; (2) measurements from the top and bottom 5 cm intervals of every u-channel that are prone to convolution effects (e.g., Oda & Xuan, 2014); (3) measurements with spurious ARM acquisition during demagnetization (recognized by substantial increase in NRM intensity during AF demagnetization); and (4) intervals with MAD and/or α_{95} values >15° associated with the six-step optimal PCA calculations. The remaining data were then subjected to (5) the Vandamme cutoff procedure (Vandamme, 1994), which iteratively determines the optimal cutoff angle and characteristic angular standard deviation of the directional distribution. This approach removes one outlier (a direction farther from the mean than the calculated optimal cutoff angle) each time until the furthest outlier was within optimal cutoff angle. We note that this procedure can mask transitional directions proximal to reversals of the geomagnetic field. Therefore, we manually examined all Zijderveld diagrams around each reversal and defined the uncertainty (i.e., transitional) interval between the first and last poorly resolved characteristic remanent magnetization direction.

Declination data from every studied core from Holes U1406A and U1406B were rotated using the FlexIT tool data (Norris et al., 2014). We also corrected the declinations of each core by rotating the core so that the circular mean of the declinations, calculated using CircStat (Berens, 2009), was oriented north or south for normal and reversed polarity zones, respectively. FlexIT tool-corrected declinations were generally very consistent with the circular-mean-oriented declinations for Holes U1406A and U1406B. Rotated declinations for Hole U1406C were only calculated using the circular-mean method, because the FlexIT tool was only deployed during the coring of Holes U1406A and U1406B (Norris et al., 2014).

3. Rock Magnetism

The selected hysteresis parameters yield good quality results (Figure 3a), despite the relatively weak remanence and strong paramagnetic component. Backfield remanence measurements suggest that a low-coercivity component with H_{cr} of ~42–53 mT dominates the samples. Slope-corrected hysteresis loops (calculated using the methods of Jackson & Solheid, 2010), however, generally do not saturate by 500 mT, indicating a potential artifact of slope correction caused by the strong paramagnetic component or at least one additional component with higher coercivity. The FORC diagrams show patterns consistent with a central ridge component, with either small interactions or none, but the ridge is very smoothed due to the ~3.5 mT field increment. No interactions may indicate highly anisotropic noninteracting single-domain magnetite, such as intact magnetosome chains (e.g., Egli et al., 2010; Roberts et al., 2013, 2014). The low-coercivity and large interaction component is consistent with the presence of a coarser-grained (i.e., a multidomain detrital) magnetic component (e.g., Roberts et al., 2012), partially collapsed magnetosome chains
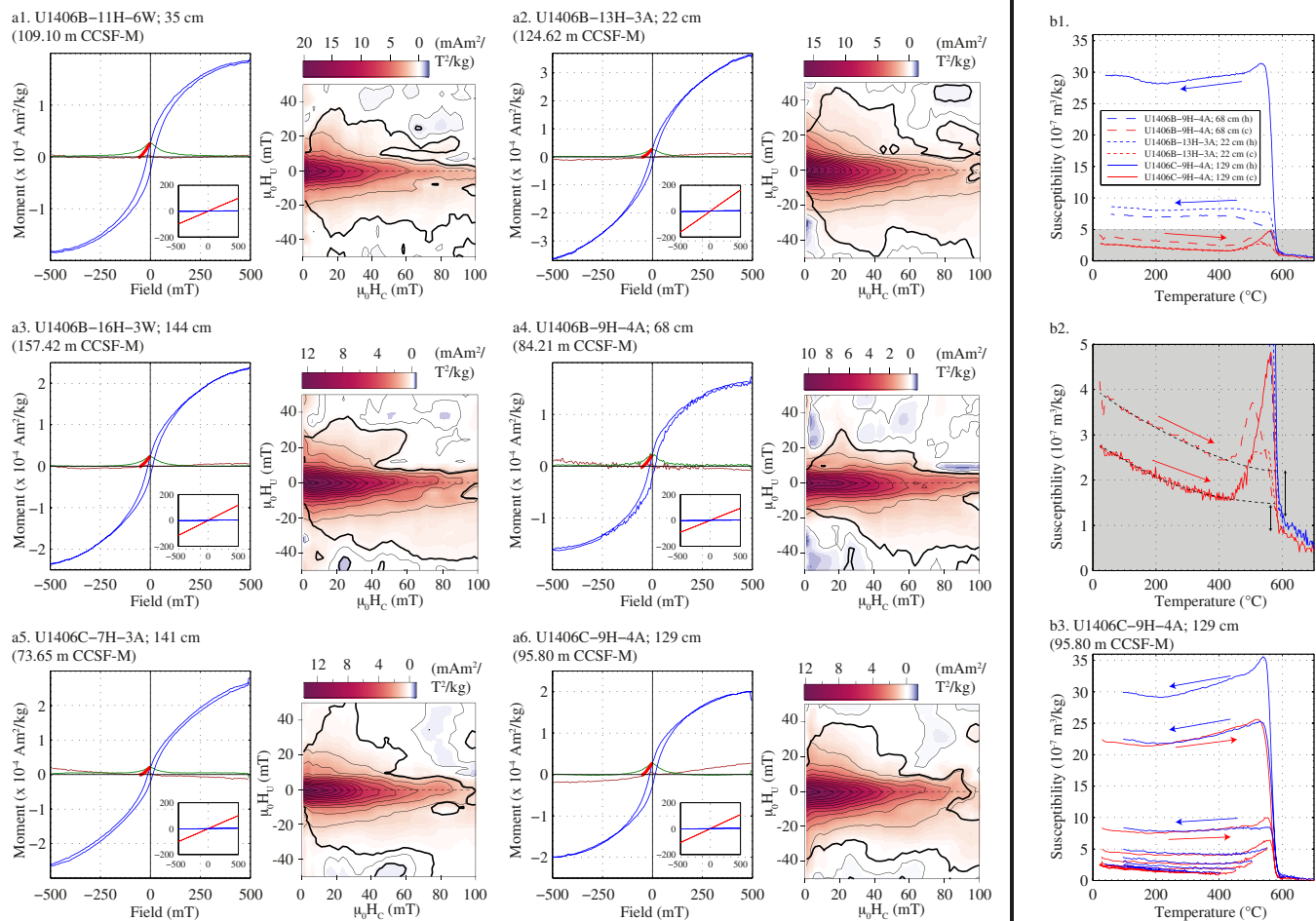
Figure 3. Examples of rock magnetic analysis results. (a1–a6) Slope-corrected hysteresis loops (blue), remanent hysteretic magnetization (green), error curve (brown), and backfield curves (thick red line) and First-Order Reversal Curve (FORC) diagrams for six representative samples. Smaller insets highlight the difference between raw (red) and drift and slope-corrected (blue) hysteresis loops using the methods of Jackson and Solheid (2010). FORC diagrams are processed using FORCinel 2.03 (Harrison & Feinberg, 2008) with VARIFORC smoothing (Egli, 2013); 95% confidence intervals (Heslop & Roberts, 2012) are represented by thick black lines. VARIFORC smoothing factors used for the FORC diagrams are $S_{c,0} = 5$–7; $S_{c,1} = 5$–8; $S_{b,0} = 3.5$–4; $S_{b,1} = 6$–8; $\lambda_c = 0.1$; $\lambda_b = 0.1$. (b1–b3) High-temperature magnetic susceptibility measurements completed in an argon atmosphere. (b2) An amplification of the warming curves only (grey shading) with vertical black arrows highlighting occurrence of magnetite. (b3) The nonreversibility of magnetic susceptibility on heating (Sample U1406C-9H-4A; 129 cm; 95.80 m CCSF-M).

(e.g., Li et al., 2012), or both. At coercivities >60 mT, all FORCs show significant positive values at negative interactions (H_u axis), but not at positive interactions (H_u axis). This is not consistent with the symmetrical signature of a pseudo-single-domain or multidomain magnetic component (e.g., Roberts et al., 2012), and it may be part of a kidney-shaped imprint that is representative of hematite or monoclinic pyrrhotite (Roberts et al., 2014).

The hyperbolic decrease in magnetic susceptibility during heating (Figure 3b) suggests the presence of a strong paramagnetic component. This observation is consistent with those from the hysteresis measurements. The hyperbolic decrease cannot be extrapolated beyond ∼590°C, suggesting the presence of magnetite, which is commonly considered a stable sedimentary remanence carrier. The increase in magnetic susceptibility at ∼500–550°C in several samples implies the formation of a new strongly magnetic component (i.e., magnetite), the presence of a Hopkinson peak (e.g., Dunlop & Özdemir, 2007), or both. Stepwise heating-cooling cycles, however, are nonreversible (Figure 3b3), suggesting that the peak in magnetic susceptibility at ∼500–550°C is caused by the formation of magnetite during heating, and hence, is not a Hopkinson peak. Destabilization of iron-bearing clay minerals may supply the iron for this magnetite that forms during the measurement process.

4. Noise-Masking Protocol and Magnetostratigraphy

4.1. Noise-Masking Protocol

PCA directions calculated using a uniform 20–60 mT demagnetization range of NRM data (raw intensity data in Supplementary information Table 1) are of highly variable quality, with a mean MAD of ∼24° (Figures 4a and 4b; Supporting information Table S2) after removing data from disturbed intervals, i.e., steps 1–3 from the aforementioned protocol. The optimized PCA directions calculated on the same measurements using the six-step combination are fairly uniformly distributed between all steps (Figure 4h, note that 65, 70, and 75 mT demagnetization steps were not used) and reduces the mean MAD to ∼11° (Figure 4a; Supporting information Table S3). Despite these optimization steps, the PCA directions still show relatively large scatter when plotted on an equal area projection (Figure 4c). This may be due to the large number of optimized PCA directions that are still associated with MAD values >15° (Figure 4a). Occasionally, optimized PCA directions with MAD values <15° can be spurious if the PCA lines do not cross near the origin (note that the origin was not anchored for PCA analyses to prevent introducing an artificially low uncertainty estimation, cf., Heslop & Roberts, 2016). In these instances, α_{95} calculated using the optimized six-step demagnetization data would be large. Thus, small values for both MAD and α_{95} are associated with the most reliable directions. The masking of all characteristic directions with MAD values >15° and/or $\alpha_{95} > 15°$ (Figure 4d) reduces the scatter of the remaining data and excludes most of the very low intensity data (Figure 4i) from which reconstructions of accurate directions is unlikely. This masking results in the retention of ∼62% of the original data set after removal of stratigraphically disturbed intervals, but a large dispersion persists (Fisher's precision parameter of the mean direction, $\kappa = \sim 6$, Figure 4e). An equal area plot of directions (Figure 4f) and a histogram of the corresponding virtual geomagnetic poles (VGPs) (Figure 4g) show that the Vandamme cutoff procedure (Vandamme, 1994) within our protocol successfully removes the remaining statistical outliers. This procedure retains the main fraction of the data (∼56% of the original data set with disturbances removed, Supporting information Table S4) close to expected values: IODP Site U1406 was at a paleolatitude of ∼34° at 25 Ma (van Hinsbergen et al., 2015), corresponding to an expected inclination of ∼±53°, assuming a geocentric axial dipole (GAD) field model.

The mean inclination within normal polarity zones becomes progressively shallower throughout the application of our protocol. The initial inclination of ∼60° (Figures 4b and 4c) is steeper than the expected ∼53° value at 25 Ma (van Hinsbergen et al., 2015). We also note that natural and coring-induced compaction commonly causes inclination shallowing (e.g., Kodama, 2012), so in the absence of steep drilling overprints, ARMs, or other directional biases, we predict that we could observe inclinations shallower than ∼53°. Indeed, this is what we observe in our normal polarity data. Mean inclination values within reversed polarity zones, however, are −36°, which are very shallow relative to the expected GAD inclination of −53° at 25 Ma (van Hinsbergen et al., 2015). We suggest that, in addition to compaction processes, the shallow inclination of reversed polarity zones probably relates to imperfect AF demagnetization of a steep downward-directed component. This is sometimes observed in the Zijderveld diagrams (Figure 5b) and also supported by the difference in average NRM intensity: the NRM intensity of some reversed polarity intervals is lower than surrounding normal polarity intervals. For example, NRM intensities within polarity zone R6 are usually lower than those in N5 and N6 (Figure 6) and NRM intensities in R14 are generally lower than those in N13 and N14 (Figure 7). This downward-directed component is too steep to be a primary magnetization but is consistent with a coring-induced magnetization (e.g., Bowles, 2007) or a spurious ARM acquired during NRM demagnetization. We limited the effects of this potential overprint on component directions by not anchoring the NRM component to the origin.

4.2. Magnetostratigraphy

Our noise-masking procedure applied to optimized PCA directions produces clearly defined reversed or normal polarity zones (designated R1-N14 in Figures 6 and 7). Data from overlapping intervals of the three holes show very consistent results. The stratigraphic uncertainties in reversal positions (Table 1) range between 4.5 and 65.5 cm (median 19 cm), compared to 4–67 cm (median 18 cm) in the shipboard data (Norris et al., 2014), excluding core gaps. The only exception is a ∼2 m uncertainty in the position of the N11/R12 reversal correlation. The magnetostratigraphic directions based on shore-based u-channel measurements, however, are of much higher precision and quality relative to the shipboard interpretation (cf., Norris et al., 2014, Figures F17–F19), notably after the masking of noisy data by the protocol. Thus, in this
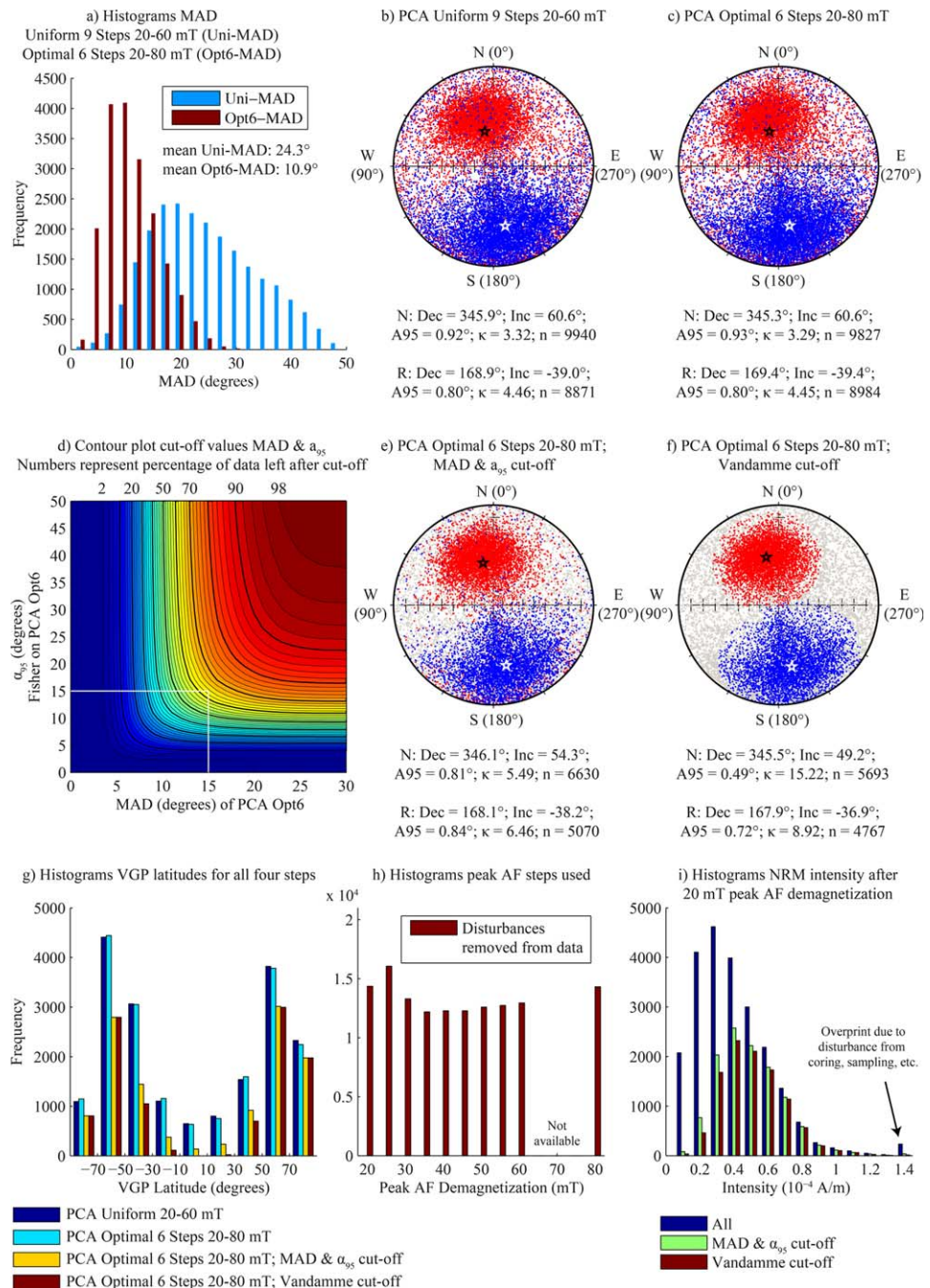
Figure 4. Noise-masking protocol applied to the natural remanent magnetization (NRM) data of Site U1406. Data from intervals with coring and sample disturbances are removed prior to the analysis. (a) Histograms of maximum angular deviation (MAD) values associated with principal component analysis (PCA) using uniform 20–60 mT and optimal six-steps in 20–80 mT AF demagnetization range. (b, c) Component directions shown on equal area projections for uniform 20–60 mT and optimal range PCA results, respectively. The optimal six-step protocol reduces the mean MAD value by one-half, but the results still show large directional scatter. (d) Contour plot showing percentages of data left for various cutoff levels of MAD and α_{95} values. (e, f) Component directions on equal area projections for the optimal range PCA results after cutoff of MAD or $\alpha_{95} > 15°$, and after the Vandamme cutoff (Vandamme, 1994), respectively. (g) Histograms of virtual geomagnetic pole (VGP) latitudes after applying each of the methods highlight the removal of low-latitude directions after application of the protocol. (h) Histograms of peak AF steps used in the optimal six-step PCA analysis, prior to and after MAD and α_{95} cutoff. (i) Histograms of intensity after 20 mT peak AF demagnetization in all data (including disturbances), and those excluding data masked by the after MAD and α_{95} cutoff, and by the Vandamme-cutoff. Note that the protocol typically removes data with low intensity and high intensity (related to various disturbances).
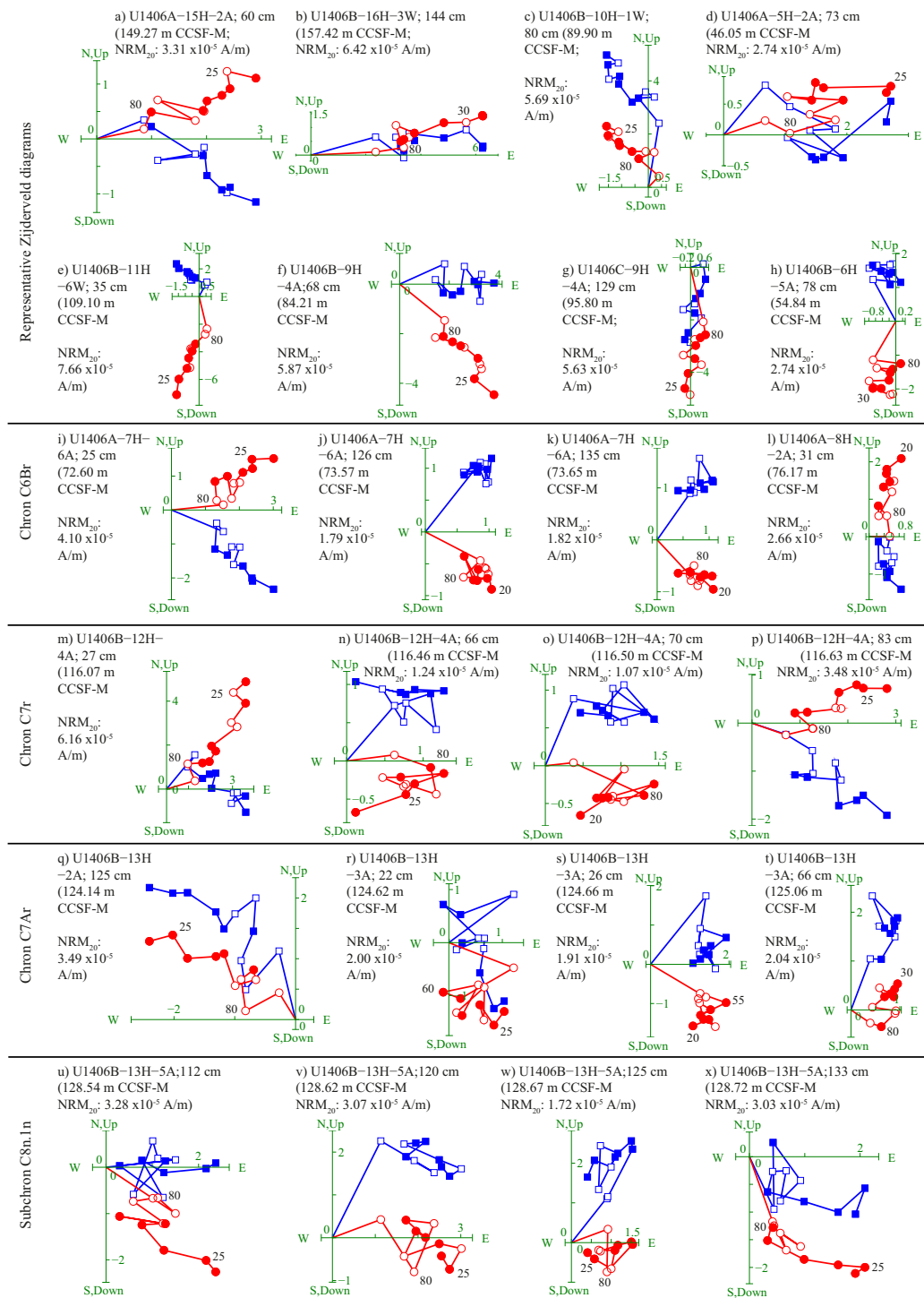
Figure 5. Zijderveld diagrams: orthogonal projection of alternating field (AF) demagnetization of u-channel samples. Natural remanent intensity after 20 mT peak AF demagnetization (NRM_{20}) is provided. The red circles and blue squares are projections on the vertical and horizontal planes, respectively. Closed circles and squares are datum points used in the optimized PCA protocol. Peak alternating fields of two demagnetization steps are indicated and axes ticks are scaled to 10^{-5} A/m. Declinations are presented in sample (unrotated) coordinates. (a–h) Representative Zijderveld diagrams; (i–x) Zijdervelds in and around intervals with rarely recorded directional changes.
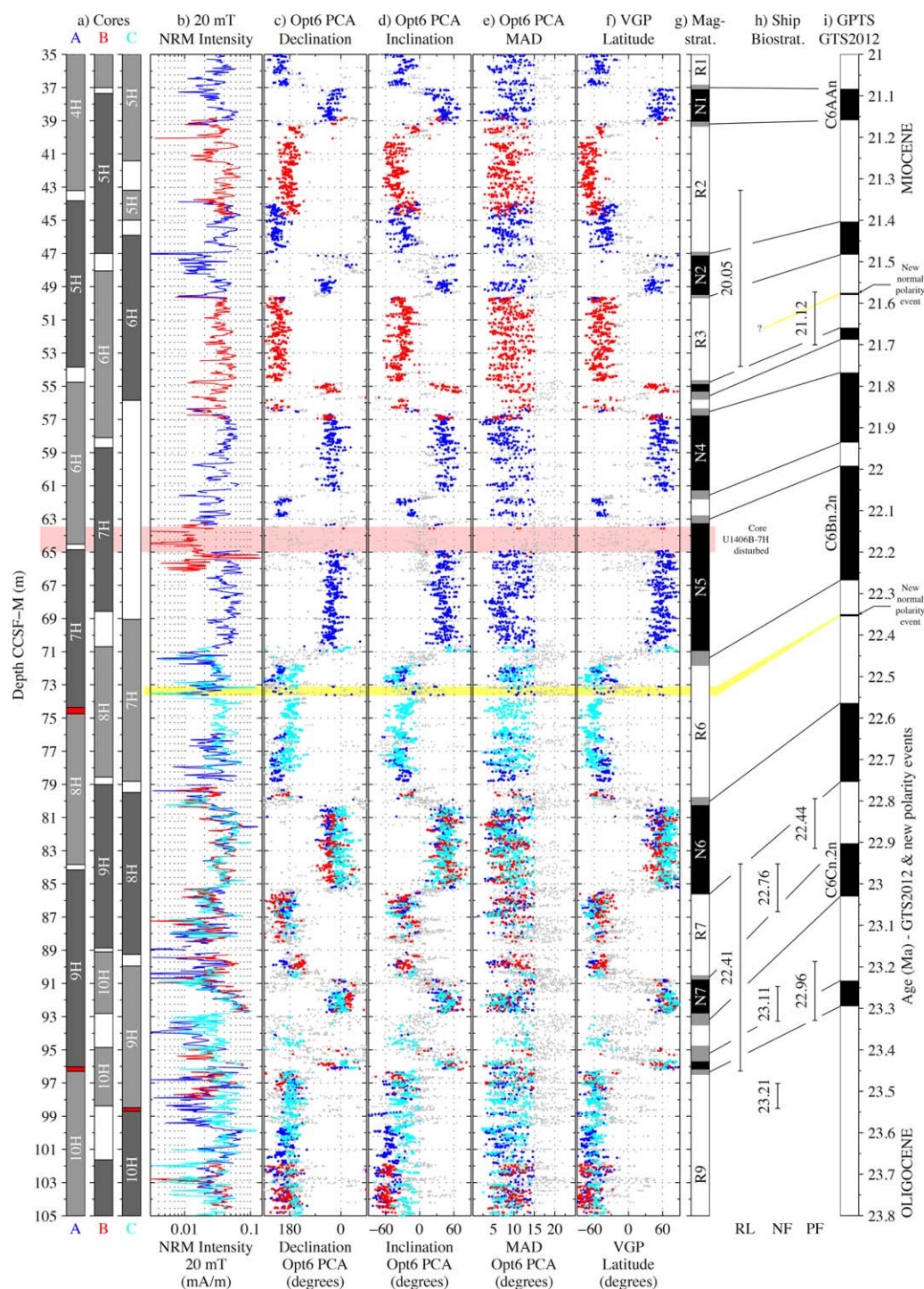
Figure 6. U-channel paleomagnetic results of IODP Site U1406 between 35 and 105 m CCSF-M. (a) Recovered cores plotted on the revised composite depth scale (van Peer et al., 2017). Natural remanent magnetization (NRM) intensities after 20 mT peak alternating field demagnetization are plotted in (b) next to the six-steps optimized principal component analysis ("Opt6 PCA") record in (c–e), including masked noisy data (in grey pluses masked by MAD and $\alpha_{95} > 15°$; grey triangles masked by Vandamme cutoff procedure). Component directions were calculated in the 20–80 mT interval. Corresponding virtual geomagnetic pole (VGP) latitudes are presented in (f). In the magnetic polarity zones in (g) black intervals represent normal polarity, white reversed, grey uncertain intervals, and are correlated to (i) of the GTS2012 (Hilgen et al., 2012; Vandenberghe et al., 2012) including rarely observed, short-duration polarity events (Channell et al., 2003, 2013; Lanci et al., 2005). (h) Selected IODP Expedition 342 shipboard biostratigraphy (Norris et al., 2014; RL is radiolaria, NF is nannofossil, PF is planktonic foraminifera) support this correlation.
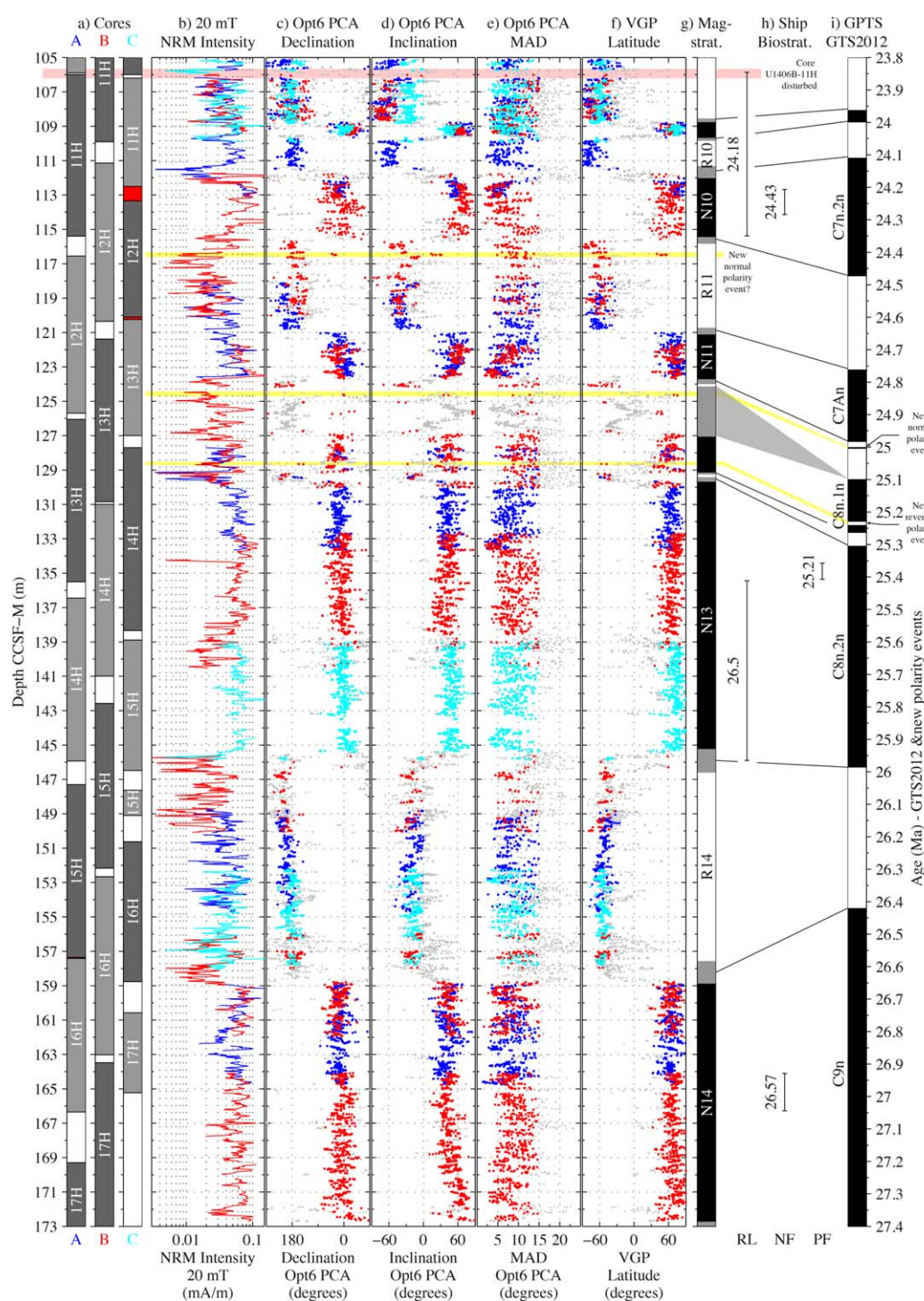
Figure 7. Interval studied with u-channel samples, 105–173 m CCSF-M. See caption for Figure 5 for details.

application to sediments recovered from IODP Site U1406, this protocol provides well-resolved magneto-stratigraphic directions. This provides the statistical background to confidently identify normal and reversed polarity zones suitable for high precision and detailed correlation to timescales and other stratigraphic records.

We revise the shipboard magnetostratigraphy (Norris et al., 2014, Table 13) by correlating zones R1 to N14 to Chrons C6Ar to C9n of the GPTS GTS2012 (Hilgen et al., 2012; Vandenberghe et al., 2012). Biostratigraphic

Table 1

Magnetostratigraphy, Integrated Ocean Drilling Program (IODP) Site U1406

Reversal	Age (Ma)	U1406A core, section, interval top	U1406A core, section, interval base	U1406A depth CSF-A (m) top	U1406A depth CSF-A (m) base	U1406A depth CCSF-M (m) top	U1406A depth CCSF-M (m) base	U1406A depth CCSF-M (m) middle	U1406A uncertainty (m)	U1406A notes
C6Ar/C6AAn	21.083	4H-3A; 51	4H-3A; 78	28.71	28.98	36.83	37.10	36.965	0.135	U-channel
C6AAn/C6AAr.1r	21.159	4H-4A; 124	4H-5A; 10	30.94	31.30	39.06	39.42	39.24	0.18	Shipboard/U-channel
C6AAr.1r/C6AAr.1n	21.403	5H-3A; 7	5H-3A; 30	37.77	38.00	46.89	47.12	47.005	0.115	U-channel
C6AAr.1n/C6AAr.2r	21.483	N.I.	N.I.	N.I.	N.I.	N.I.	N.I.	N.I.	N.I.	
C6AAr.2r/C6AAr.2n	21.659	N.I.	N.I.	N.I.	N.I.	N.I.	N.I.	N.I.	N.I.	
C6AAr.2n/C6AAr.3r	21.688	N.I.	N.I.	N.I.	N.I.	N.I.	N.I.	N.I.	N.I.	
C6AAr.3r/C6Bn.1n	21.767	6H-2A; 22.5	6H-3A; 50	45.925	47.70	56.485	58.26	57.3725	0.8875	Shipboard/U-channel
C6Bn.1n/C6Bn.1r	21.936	6H-5A; 52	6H-5A; 106	50.72	51.26	61.28	61.82	61.55	0.27	U-channel
C6Bn.1r/C6Bn.2n	21.992	6H-6A; 53	6H-6A; 100	52.23	52.70	62.79	63.26	63.025	0.235	U-channel
C6Bn.2n/C6Br	22.268	7H-5A; 10	7H-5A; 99	59.8	60.69	70.96	71.85	71.405	0.445	U-channel
C6Br/C6Br.1n*	~22.331	7H-6A; 47	7H-6A; 124	61.67	62.44	72.81	73.55	73.18	0.37	U-channel
C6Br.1n*/C6Br	~22.354	N.I.	N.I.	N.I.	N.I.	N.I.	N.I.	N.I.	N.I.	
C6Br/C6Cn.1n	22.564	8H-4A; 10	8H-4A; 139	67.8	69.09	78.96	80.25	79.605	0.645	U-channel
C6Cn.1n/C6Cn.1r	22.754	9H-1W; 145	9H-2A; 22	74.15	74.42	85.61	85.88	85.745	0.135	U-channel
C6Cn.1r/C6Cn.2n	22.902	9H-4A; 137	9H-5A; 58	78.58	79.3	90.04	90.76	90.4	0.36	U-channel
C6Cn.2n/C6Cn.2r	23.030	N.I.	N.I.	N.I.	N.I.	N.I.	N.I.	N.I.	N.I.	
C6Cn.2r/C6Cn.3n	23.233	N.I.	N.I.	N.I.	N.I.	N.I.	N.I.	N.I.	N.I.	
C6Cn.3n/C6Cr	23.295	9H-7W; 56	10H-1A; 36	82.32	82.56	96.11	96.39	96.25	0.14	U-channel
C6Cr/C7n.1n	23.962	11H-2A; 137	11H-3A; 7	94.57	94.77	108.55	108.76	108.655	0.105	U-channel
C7n.1n/C7n.1r	24.000	11H-3A; 100	11H-3A; 117	95.7	95.87	109.68	109.85	109.765	0.085	U-channel
C7n.1r/C7n.2n	24.109	11H-4A; 114	11H-5A; 34	97.34	98.04	111.32	112.02	111.67	0.35	U-channel
C7n.2n/C7r	24.474	N.I.	N.I.	N.I.	N.I.	N.I.	N.I.	N.I.	N.I.	
C7r/C7r.1n*	~24.509	N.I.	N.I.	N.I.	N.I.	N.I.	N.I.	N.I.	N.I.	
C7r.1n*/C7r	~24.525	N.I.	N.I.	N.I.	N.I.	N.I.	N.I.	N.I.	N.I.	
C7r/C7An	24.761	12H-3A; 138	12H-4A; 21	105.58	105.91	120.78	121.11	120.945	0.165	U-channel
C7An/C7Ar	24.984	12H-5A; 127	12H-6A; 20	108.47	108.8	123.51	123.76	123.635	0.125	U-channel/shipboard
C7Ar/C7Ar.1n*	~24.997	N.I.	N.I.	N.I.	N.I.	N.I.	N.I.	N.I.	N.I.	
C7Ar.1n*/C7Ar	~25.023	N.I.	N.I.	N.I.	N.I.	N.I.	N.I.	N.I.	N.I.	
C7Ar/C8n.1n	25.099	N.I.	N.I.	N.I.	N.I.	N.I.	N.I.	N.I.	N.I.	
C8n.1n/C8n.1r	25.264	N.I.	N.I.	N.I.	N.I.	N.I.	N.I.	N.I.	N.I.	
C8n.1r/C8n.2n	25.304	N.I.	N.I.	N.I.	N.I.	N.I.	N.I.	N.I.	N.I.	
C8n.2n/C8r	25.987	N.I.	N.I.	N.I.	N.I.	N.I.	N.I.	N.I.	N.I.	
C8r/C9n	26.420	16H-1A; 117.5	16H-2A; 10	140.38	140.80	158.53	158.95	158.74	0.21	Shipboard
C9n/C9r	27.439	N.I.	N.I.	N.I.	N.I.	N.I.	N.I.	N.I.	N.I.	

Reversal	Age (Ma)	U1406B core, section, interval top	U1406B core, section, interval base	U1406B depth CSF-A (m) top	U1406B depth CSF-A (m) base	U1406B depth CCSF-M (m) top	U1406B depth CCSF-M (m) base	U1406B depth CCSF-M (m) middle	U1406B uncertainty (m)	U1406B notes
C6Ar/C6AAn	21.083	N.I.	N.I.	N.I.	N.I.	N.I.	N.I.	N.I.	N.I.	
C6AAn/C6AAr.1r	21.159	5H-2A; 14	5H-2A; 64	31.46	31.94	38.88	39.36	39.12	0.24	U-channel
C6AAr.1r/C6AAr.1n	21.403	5H-7A; 45	6H-1A; 10	39.15	39.40	46.519	48.16	47.3395	0.8205	Shipboard
C6AAr.1n/C6AAr.2r	21.483	6H-1W; 144	6H-2A; 14	40.74	40.94	49.50	49.70	49.6	0.1	U-channel
C6AAr.2r/C6AAr.2n	21.659	6H-5A; 57	6H-5A; 81	45.87	46.11	54.63	54.87	54.75	0.12	U-channel
C6AAr.2n/C6AAr.3r	21.688	6H-5A; 127	6H-6A; 25	46.57	47.05	55.33	55.81	55.57	0.24	U-channel
C6AAr.3r/C6Bn.1n	21.767	6H-6A; 78	6H-6A; 120	47.58	48.00	56.34	56.76	56.55	0.21	U-channel
C6Bn.1n/C6Bn.1r	21.936	N.I.	N.I.	N.I.	N.I.	N.I.	N.I.	N.I.	N.I.	
C6Bn.1r/C6Bn.2n	21.992	N.I.	N.I.	N.I.	N.I.	N.I.	N.I.	N.I.	N.I.	
C6Bn.2n/C6Br	22.268	N.I.	N.I.	N.I.	N.I.	N.I.	N.I.	N.I.	N.I.	
C6Br/C6Br.1n*	~22.331	N.I.	N.I.	N.I.	N.I.	N.I.	N.I.	N.I.	N.I.	
C6Br.1n*/C6Br	~22.354	N.I.	N.I.	N.I.	N.I.	N.I.	N.I.	N.I.	N.I.	
C6Br/C6Cn.1n	22.564	9H-1W; 85	9H-1W; 145	68.65	69.25	79.76	80.46	80.11	0.35	U-channel
C6Cn.1n/C6Cn.1r	22.754	9H-4A; 146	9H-5A; 62	73.78	74.45	84.99	85.66	85.325	0.335	U-channel
C6Cn.1r/C6Cn.2n	22.902	10H-1W; 81	10H-2W; 51	78.11	79.31	89.91	91.11	90.51	0.6	U-channel
C6Cn.2n/C6Cn.2r	23.030	N.I.	N.I.	N.I.	N.I.	N.I.	N.I.	N.I.	N.I.	
C6Cn.2r/C6Cn.3n	23.233	N.I.	N.I.	N.I.	N.I.	N.I.	N.I.	N.I.	N.I.	
C6Cn.3n/C6Cr	23.295	10H-4A; 52	10H-4A; 75	82.34	82.57	96.19	96.42	96.305	0.115	U-channel
C6Cr/C7n.1n	23.962	11H-5A; 124	11H-5A; 146	94.04	94.26	108.65	108.81	108.73	0.08	U-channel
C7n.1n/C7n.1r	24.000	11H-6W; 87	11H-6W; 113	95.17	95.43	109.49	109.68	109.585	0.095	U-channel

Table 1. *(continued)*

Reversal	Age (Ma)	U1406B core, section, interval top	U1406B core, section, interval base	U1406B depth CSF-A (m) top	U1406B depth CSF-A (m) base	U1406B depth CCSF-M (m) top	U1406B depth CCSF-M (m) base	U1406B depth CCSF-M (m) middle	U1406B uncertainty (m)	U1406B notes
C7n.1r/C7n.2n	24.109	11H-6W; 135	12H-1W; 36	95.65	96.66	109.85	111.54	110.695	0.845	U-channel
C7n.2n/C7r	24.474	12H-3A; 115	12H-4A; 4	100.46	100.86	115.44	115.84	115.64	0.2	U-channel
C7r/C7r.1n*	~24.509	12H-4A; 29	12H-4A; 65	101.11	101.47	116.09	116.45	116.27	0.18	U-channel
C7r.1n*/C7r	~24.525	12H-4A; 71	12H-4A; 80	101.53	101.62	116.51	116.6	116.555	0.045	U-channel
C7r/C7An	24.761	12H-6A; 121	13H-1A; 20	105.05	105.7	119.96	121.58	120.77	0.81	U-channel
C7An/C7Ar	24.984	13H-2A; 83	13H-2A; 110	107.84	108.12	123.72	124	123.86	0.14	U-channel
C7Ar/C7Ar.1n*	~24.997	13H-2A; 125	13H-2A; 140	108.26	108.41	124.14	124.29	124.215	0.075	U-channel
C7Ar.1n*/C7Ar	~25.023	13H-3A; 32	13H-3A; 74	108.84	109.26	124.72	125.14	124.93	0.21	U-channel
C7Ar/C8n.1n	25.099	13H-3A; 74	13H-4A; 114	109.26	111.17	125.14	127.05	126.095	0.955	U-channel
C8n.1n/C8n.1r	25.264	13H-6A; 22	13H-6A; 38	113.27	113.39	129.15	129.27	129.21	0.06	U-channel
C8n.1r/C8n.2n	25.304	13H-6A; 48	13H-6A; 76	113.53	113.81	129.41	129.67	129.54	0.13	U-channel
C8n.2n/C8r	25.987	15H-2A; 112.5	15H-3A; 103	127.13	128.53	145.21	146.61	145.91	0.7	Shipboard/U-channel
C8r/C9n	26.420	16H-4A; 7	16H-4A; 137	138.6	139.9	157.57	158.88	158.225	0.655	U-channel
C9n/C9r	27.439	N.I.	N.I.	N.I.	N.I.	N.I.	N.I.	N.I.	N.I.	

Reversal	Age (Ma)	U1406C core, section, interval top	U1406C core, section, interval base	U1406C depth CSF-A (m) top	U1406C depth CSF-A (m) base	U1406C depth CCSF-M (m) top	U1406C depth CCSF-M (m) base	U1406C depth CCSF-M (m) middle	U1406C uncertainty (m)	U1406C notes
C6Ar/C6AAn	21.083	N.I.	N.I.	N.I.	N.I.	N.I.	N.I.	N.I.	N.I.	
C6AAn/C6AAr.1r	21.159	N.I.	N.I.	N.I.	N.I.	N.I.	N.I.	N.I.	N.I.	
C6AAr.1r/C6AAr.1n	21.403	N.I.	N.I.	N.I.	N.I.	N.I.	N.I.	N.I.	N.I.	
C6AAr.1n/C6AAr.2r	21.483	N.I.	N.I.	N.I.	N.I.	N.I.	N.I.	N.I.	N.I.	
C6AAr.2r/C6AAr.2n	21.659	N.I.	N.I.	N.I.	N.I.	N.I.	N.I.	N.I.	N.I.	
C6AAr.2n/C6AAr.3r	21.688	N.I.	N.I.	N.I.	N.I.	N.I.	N.I.	N.I.	N.I.	
C6AAr.3r/C6Bn.1n	21.767	N.I.	N.I.	N.I.	N.I.	N.I.	N.I.	N.I.	N.I.	
C6Bn.1n/C6Bn.1r	21.936	N.I.	N.I.	N.I.	N.I.	N.I.	N.I.	N.I.	N.I.	
C6Bn.1r/C6Bn.2n	21.992	N.I.	N.I.	N.I.	N.I.	N.I.	N.I.	N.I.	N.I.	
C6Bn.2n/C6Br	22.268	7H-2A; 30	7H-2A; 135	52.2	53.25	70.96	72.08	71.52	0.56	U-channel
C6Br/C6Br.1n*	~22.331	7H-3A; 83	7H-3A; 140	54.23	54.8	73.07	73.64	73.355	0.285	U-channel
C6Br.1n*/C6Br	~22.354	7H-3A; 147	7H-4A; 11	54.87	55.01	73.72	73.85	73.785	0.065	U-channel
C6Br/C6Cn.1n	22.564	7H-6A; 149	8H-1A; 75	59.39	60.65	78.23	80.37	79.3	1.07	U-channel
C6Cn.1n/C6Cn.1r	22.754	8H-4A; 113	8H-5A; 37	65.53	66.27	85.21	85.93	85.57	0.36	U-channel
C6Cn.1r/C6Cn.2n	22.902	9H-1A; 74	9H-2A; 29	70.14	71.19	90.58	91.53	91.055	0.475	U-channel
C6Cn.2n/C6Cn.2r	23.030	9H-3A; 7	9H-3A; 78	72.47	73.18	92.81	93.52	93.165	0.355	U-channel
C6Cn.2r/C6Cn.3n	23.233	9H-4A; 50	9H-4A; 116	74.4	75.06	94.75	95.69	95.22	0.47	U-channel
C6Cn.3n/C6Cr	23.295	9H-5A; 16	9H-5A; 49	75.56	75.89	96.12	96.4	96.26	0.14	U-channel
C6Cr/C7n.1n	23.962	11H-3W; 140	11H-4A; 12	92.8	93.02	108.82	108.94	108.88	0.06	U-channel
C7n.1n/C7n.1r	24.000	11H-4A; 114	11H-4A; 136	93.94	94.26	109.54	109.84	109.69	0.15	U-channel
C7n.1r/C7n.2n	24.109	11H-5A; 110	11H-6A; 17.5	95.50	96.08	111.02	111.57	111.295	0.275	Shipboard
C7n.2n/C7r	24.474	12H-4A; 92.5	12H-4A; 102.5	103.33	103.43	115.61	115.71	115.66	0.05	Shipboard
C7r/C7r.1n*	~24.509	N.I.	N.I.	N.I.	N.I.	N.I.	N.I.	N.I.	N.I.	
C7r.1n*/C7r	~24.525	N.I.	N.I.	N.I.	N.I.	N.I.	N.I.	N.I.	N.I.	
C7r/C7An	24.761	13H-2A; 10	13H-3A; 20	108.76	109.17	121.6	122.01	121.805	0.205	Shipboard
C7An/C7Ar	24.984	13H-4A; 47.5	13H-4A; 62.5	110.95	111.10	123.49	123.61	123.55	0.06	Shipboard
C7Ar/C7Ar.1n*	~24.997	N.I.	N.I.	N.I.	N.I.	N.I.	N.I.	N.I.	N.I.	
C7Ar.1n*/C7Ar	~25.023	N.I.	N.I.	N.I.	N.I.	N.I.	N.I.	N.I.	N.I.	
C7Ar/C8n.1n	25.099	N.I.	N.I.	N.I.	N.I.	N.I.	N.I.	N.I.	N.I.	
C8n.1n/C8n.1r	25.264	N.I.	N.I.	N.I.	N.I.	N.I.	N.I.	N.I.	N.I.	
C8n.1r/C8n.2n	25.304	N.I.	N.I.	N.I.	N.I.	N.I.	N.I.	N.I.	N.I.	
C8n.2n/C8r	25.987	15H-5A; 74	15H-5A; 25	133.14	134.15	145.23	146.12	145.675	0.445	U-channel/shipboard
C8r/C9n	26.420	N.I.	N.I.	N.I.	N.I.	N.I.	N.I.	N.I.	N.I.	
C9n/C9r	27.439	N.I.	N.I.	N.I.	N.I.	N.I.	N.I.	N.I.	N.I.	

Note: Depths (on CCSF-M depth scale, cf., van Peer et al., 2017) of all reversals identified at IODP Site U1406. Reversal ages from Hilgen et al. (2012) and Vandenberghe et al. (2012). Reversal ages of the rarely observed, short-duration polarity events (highlighted with *) in Chron C6Br, C7r, and C7Ar are estimated using linear interpolation. See text for details. Notes indicate whether the depths of identified reversals are (partially) based on shore-based, u-channel sample, or shipboard, half-core data (Norris et al., 2014). N.I. is not identified.

events (Table 2) support this correlation and primarily consist of the shipboard identification of the occurrences of nannofossils *Sphenolithus belemnos*, *Sphenolithus delphix*, and *Sphenolithus distentus*, and planktonic foraminifer *Paragloborotalia kugleri* (Norris et al., 2014). The correlation of zones R1–R2 to Chrons C6Ar and C6AAr.1r, however, is not consistent with the shipboard identification of the Base of *S. belemnos* (~19.03 Ma, Hilgen et al., 2012) in Core sections U1406A-4H-CC and U1406B-4H-CC (Norris et al., 2014). Reanalysis of the shipboard calcareous nannofossil stratigraphy in these and surrounding samples moves the Base of *S. belemnos* to Sample U1406A-4H-1W; 75 cm (34.07 m CCSF-M, Table 2). This position is above the strongly developed glauconite horizon, and thus this glauconite horizon occurs between the C6Ar/ C6AAn reversal (~21.083 Ma, Hilgen et al., 2012) and the Base of *S. belemnos* (~19.03 Ma, Hilgen et al., 2012). We therefore interpret this glauconite horizon as a ~2 Myr stratigraphic hiatus. Shipboard operations identified microfaults, as well as disrupted and contorted bedding, within Cores U1406A-17H, U1406B-18H, and U1406C-17H, which were interpreted to indicate slumping (Norris et al., 2014). We correlate this interval to the middle Oligocene, and notably, Chrons C9r and C10n are missing within this interval (Norris et al., 2014). The results presented here corroborate shipboard results (Norris et al., 2014) that interpreted a ~2 Myr-long hiatus (~27–29 Ma) in these cores.

The magnetostratigraphic framework also provides the high-fidelity age control required for environmental and paleoclimatic studies of the OMT interval. This framework resolves inconsistencies in the shipboard identification of the C6Cn reversals (Norris et al., 2014) through the correlation of zones N6 to N8 to the three normal subchrons of Chron C6Cn. In addition, we identify putative normal polarity intervals (Table 1) within Chrons C6Br (~73.5 m CCSF-M), C7r (~116.4 m CCSF-M), and C7Ar (~124.5 m CCSF-M), and tentatively identify a short-duration interval of reversed polarity within Subchron C8n.1n (~128.65 m CCSF-M).

We calculate sedimentation rates (Figure 8) based on the correlation of the Site U1406 magnetostratigraphy (Table 1) to the Geological Time Scale 2012 (GTS2012, Hilgen et al., 2012; Vandenberghe et al., 2012). The Miocene interval of this record (~35–95 m CCSF-M; ~21–23 Ma) has the highest linear sedimentation rate (LSR) of the studied interval, with values up to ~3 cm/kyr, apart from Subchron C6AAr.3r when LSR is ~0.9 cm/kyr. Within the Oligocene part of the record (~95–175 m CCSF-M; ~23–27 Ma) LSR gradually decreases from ~2.5 cm/kyr above the slump to ~1 cm/kyr in Subchron C6Cn.2r (latest Oligocene), except during Subchrons C7n.1n (LSR ~2.9 cm/kyr) and C8n.1r (LSR ~0.8 cm/kyr).

5. Discussion

5.1. Occurrence of Rarely Recorded Geomagnetic Events

The moderate LSR (average 2.3 cm/kyr) calculated at IODP Site U1406 makes it adequate for recording chrons, subchrons, and possibly some short-duration geomagnetic events (e.g., Roberts & Winklhofer, 2004). Short-duration events were originally labeled cryptochrons after identification in marine magnetic anomaly (MMA) profiles (e.g., Cande & Kent, 1992, 1995; LaBrecque et al., 1977) and may represent either brief periods of low geomagnetic field intensity (Cande & LaBrecque, 1974), or short polarity intervals (Blakely, 1974). These events can be classed as subchrons (cf., Cande & Kent, 1992) once such short-duration directional changes are globally identified and include two well-characterized geomagnetic polarity reversals. A more detailed description of the frequency of the occurrence of short-duration events may help with a more fundamental understanding of geodynamo processes; for example, why does the geomagnetic field reverse at irregular or on very short time intervals?

Several short-duration, rarely recorded geomagnetic events have been previously reported during Subchrons C6AAr.2r and C8n.1n, and Chrons C6Br and C7Ar at South Atlantic Ocean ODP Site 1090 and at equatorial Pacific Ocean ODP Site 1218 and IODP Site U1334 (Channell et al., 2003, 2013; Lanci et al., 2005; Figures 6 and 7). However, the relatively stratigraphically condensed character of these sites (average sedimentation rates 1–1.5 cm/kyr) makes it difficult to obtain a complete inventory of short-duration geomagnetic events during the Oligocene to Miocene epochs, and at present, these potential geomagnetic events are observed only in these records. Site U1406 has a higher LSR (up to ~3 cm/kyr over the studied interval) and may therefore be better suited to record short-duration geomagnetic events than the records from the Pacific and South Atlantic Ocean. We can thus use the detailed magnetostratigraphy from Site U1406 to test the fidelity of previously published magnetostratigraphic records, including these rarely observed geomagnetic events.

Table 2
Biostratigraphy, Integrated Ocean Drilling Program (IODP) Site U1406

Datum	Top					Base					Middle			Comments
	Hole, core, type, section	Interval (cm)	Depth CSF-A (m)	Depth revised CCSF-A (m)	Depth CCSF-M (m)	Hole, core, type, section	Interval (cm)	Depth CSF-A (m)	Depth revised CCSF-A (m)	Depth CCSF-M (m)	Middle CCSF-M (m)	Uncertainty (m)	Age (Ma)	
B Sphenolithus belemnos	U1406A-4H-1	75	25.95	34.07	34.07	U1406A-4H-3	75	28.95	37.07	37.07	35.57	1.50	19.03	Reanalyzed. Different from shipboard report (Norris et al., 2014)
B Sphenolithus disbelemnos	U1406A-8H-7	0	72.63	83.79	83.79	U1406A-9H-2	100	75.21	86.67	86.67	85.23	1.44	22.76	
T Sphenolithus capricornutus	U1406A-9H-5	100	79.72	91.18	91.18	U1406A-9H-6	88	81.12	92.58	93.26	92.22	1.04	22.97	
T Sphenolithus delphix	U1406A-9H-5	100	79.72	91.18	91.18	U1406A-9H-6	88	81.12	92.58	93.26	92.22	1.04	23.11	
B Sphenolithus delphix	U1406A-10H-1	100	83.20	97.03	97.03	U1406A-10H-2	100	84.70	98.53	98.53	97.78	0.75	23.21	
T Sphenolithus ciperoensis	U1406A-11H-5	100	98.70	112.68	112.68	U1406A-11H-6	100	100.22	114.20	114.14	113.41	0.73	24.43	
T Sphenolithus distentus	U1406A-16H-5	75	145.95	164.10	164.10	U1406A-16H-CC	0	148.04	166.19	166.29	165.19	1.09	26.44	
Bc Triquetrorhabdulus carinatus	U1406A-16H-5	75	145.95	164.10	164.10	U1406A-16H-CC	0	148.04	166.19	166.29	165.19	1.09	26.57	
B Sphenolithus ciperoensis	U1406A-18H-1	75	158.05	185.22	185.22	U1406A-18H-3	75	160.89	188.06	188.06	186.64	1.42	29.62	
B Sphenolithus distentus	U1406A-19H-2	75	166.95	200.22	198.85	U1406A-19H-3	75	168.45	201.72	200.05	199.45	0.60	30.00	
B Dorcadospyris dentata	U1406A-3H-CC	0	25.49	34.06	33.18	U1406A-4H-CC	0	35.07	43.19	43.19	38.19	5.00	18.22	
T Dorcadospyris ateuchus	U1406A-3H-CC	0	25.49	34.06	33.18	U1406A-4H-CC	0	35.07	43.19	43.19	38.19	5.00	18.64	
T Theocyrtis annosa	U1406A-4H-CC	0	35.07	43.19	43.19	U1406A-5H-CC	0	44.43	53.55	53.81	48.50	5.31	20.05	
B Cyrtocapsa tetrapera	U1406A-8H-7	0	72.63	83.79	83.79	U1406A-9H-CC	0	82.64	94.10	96.28	90.03	6.24	21.82	
T Artophormis gracilis	U1406A-8H-7	0	72.63	83.79	83.79	U1406A-9H-CC	0	82.64	94.10	96.28	90.03	6.24	22.41	
B Lychnocanoma elongata	U1406A-10H-7	0	91.65	105.48	105.87	U1406A-11H-CC	0	101.52	115.50	115.38	110.62	4.76	24.18	
B Lychnocanoma apadora	U1406A-13H-7	0	120.06	135.61	135.44	U1406A-14H-CC	0	128.55	144.60	145.90	140.67	5.23	26.50	
T Paragloborotalia kugleri	U1406A-5H-5	100	40.20	49.32	49.32	U1406A-5H-6	100	43.20	52.32	52.50	50.91	1.59	21.12	
T Globoquadrina dehiscens	U1406A-8H-4	100	68.70	79.86	79.86	U1406A-8H-6	100	71.70	82.86	82.86	81.36	1.50	22.44	
B Paragloborotalia kugleri	U1406A-9H-4	100	78.21	89.67	89.67	U1406A-9H-6	88	81.11	92.57	93.23	91.45	1.78	22.96	
B Paragloborotalia pseudokugleri	U1406A-13H-6	75	118.96	134.51	134.42	U1406A-13H-7	0	119.98	135.53	135.36	134.89	0.47	25.21	
B Globoturborotalita angulisuturalis	U1406A-17H-3	46	151.56	172.26	172.26	U1406A-17H-5	91	155.01	175.71	175.71	173.99	1.72	29.18	
T Turborotalia ampliapertura	U1406A-18H-2	45	159.09	186.26	186.26	U1406A-18H-4	60	162.24	189.41	189.38	187.82	1.56	30.28	

Note: Depths (on CCSF-M depth scale, cf., van Peer et al., 2017) of all shipboard biostratigraphic events identified at IODP Site U1406 and the reanalysis of nannofossil *Sphenolithus belemnos*. Ages of biostratigraphic datums from Hilgen et al. (2012) and Vandenberghe et al. (2012).
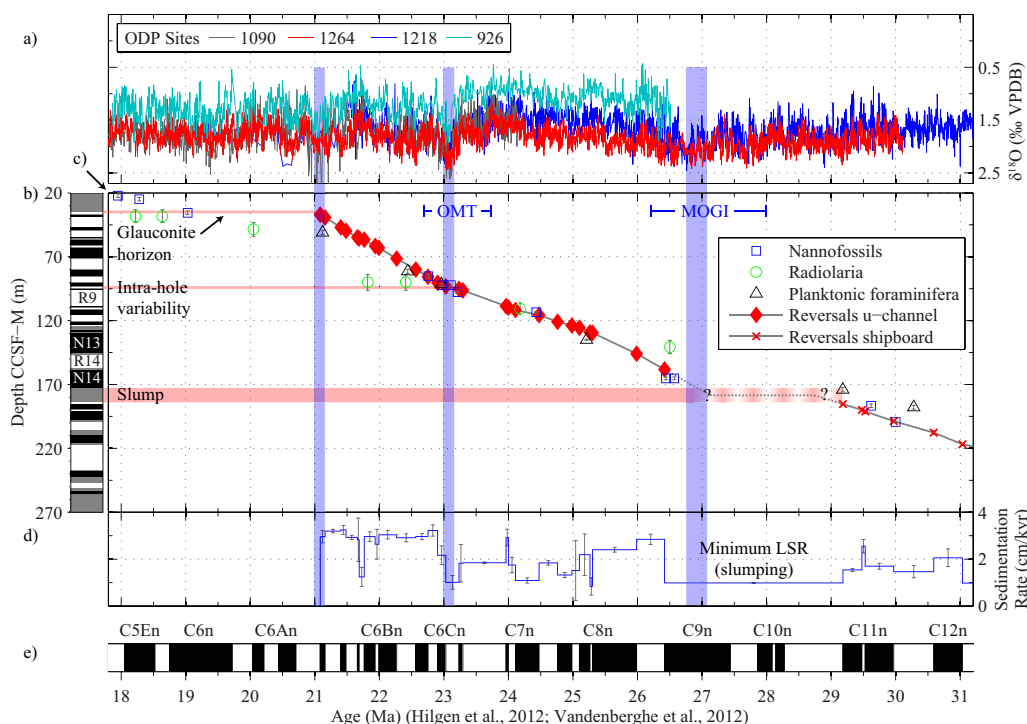
Figure 8. Stratigraphic framework of IODP Site U1406. Intervals of stratigraphic complexities, indicated by red horizontal bars, occur during global cold periods interpreted from $\delta^{18}O$ records from (a) ODP Sites 926, 1090, 1218, and 1264 (Billups et al., 2004; Liebrand et al., 2016; Pälike et al., 2006a, 2006b). Timing of the Oligocene-Miocene Transition (OMT) and Mid-Oligocene Glacial Interval (MOGI) intervals follow Liebrand et al. (2017). (b) The magnetostratigraphy for IODP Site U1406 from this study. Magnetobiostratigraphic tie points are plotted in (c), and our correlation to the geomagnetic polarity time scale (Hilgen et al., 2012; Vandenberghe et al., 2012) in (e). Calculated linear sedimentation rates, with uncertainties propagating from the depth domain, are shown in (d).

At IODP Site U1406, we observe similar short-duration intervals of normal polarity within Chrons C6Br and C7Ar (Figures 5i–5l and 5q–5t, yellow shaded bars in Figures 6 and 7), similar to Channell et al. (2003, 2013) and Lanci et al. (2005), and also, for the first time in a sedimentary record, in Chron C7r (Figures 5m–5p, yellow shaded bars in Figures 6 and 7). However, evidence for a potential reversed polarity interval during Subchron C8n.1n is less clear (Figures 5u–5x), and Subchron C6AAr.2r does not contain an interval of normal polarity, in contrast to previous reports from Site U1334 that identified a new polarity interval in Subchron C6AAr.2r (Channell et al., 2013). Preliminary rock magnetic experiments indicate that these short intervals of normal polarity do not correspond to anomalous rock magnetic or lithostratigraphic properties (e.g., Figure 3, Sample U1406B-13H-3A, 22 cm is in the middle of the normal polarity interval within Chron C7Ar, Zijderveld diagram in Figure 5r). Therefore, we conclude that these short-duration changes in magnetic polarity are not caused by a change in magnetic or sediment characteristics (e.g., mineralogy or grain-size) but reflect genuine features of the geomagnetic field. In total, we observe three new short-duration polarity intervals with high confidence and tentatively identify a fourth interval at Site U1406.

The short polarity change in Chron C6Br occurs at ~73.5 m CCSF-M in both Holes U1406A (Figures 5i–5l) and U1406C (Figure 6). This interval is present between 22.331 and 22.354 Ma (Table 1), based on linear interpolation between the reversal boundaries of Chron C6Br using the GTS2012 age model (Hilgen et al., 2012). Another short-duration polarity change occurs at ~12% from the top of Chron C7r (~116.4 m CCSF-M, Figures 5m–5p and 6), with its top and bottom reversals at 24.509 and 24.525 Ma (Table 1). A cryptochron is present in the middle of Chron C7r in MMA profiles from the North Pacific (Cande & Kent, 1992), but this has never been unequivocally demonstrated to reflect directional variability. Thus, the interval of normal polarity within Chron C7r at Site U1406 may be the same geomagnetic feature as observed in MMA profiles if the sedimentation rate at Site U1406, the spreading rate in the North Pacific, or both, varied substantially throughout Chron C7r. Testing this correlation will require further work on the integration of the

MMA profiles and the sedimentary record of Site U1406, such as the use of relative paleointensity to exclude variability in field intensity or astronomical tuning to provide alternative age control.

The third anomalous short-duration polarity interval observed at Site U1406 occurs within Chron C7Ar (Table 1 and Figures 5q–5t and 7). A complex sequence of paleomagnetic directions, present in Core U1406B-13H, hampers straightforward interpretation. Most of Chron C7Ar consists of an interval of uncertain polarity with southward-directed declination and positive inclination (~125–127 m CCSF-M). The last step of our protocol, the Vandamme cutoff (Vandamme, 1994), masks almost all directions in this uncertain interval. The top of Chron C7Ar, however, consists of a ~1.3 m thick interval of reversed polarity in which a ~0.7 m thick interval of normal polarity is present at ~124.5 m CCSF-M. Zijderveld diagrams of Core U1406B-13H demonstrate that this normal polarity event within C7Ar is not part of the interval of uncertain polarity but instead represents a genuine feature of the geomagnetic field (Figures 5q–5t). We estimate the age of the normal polarity event boundaries in Chron C7Ar to 24.997 and 25.023 Ma (Table 1). Another possible, rarely observed polarity event may be present in Chron C8n.1n at ~128.65 m CCSF-M, but it is not clearly expressed at IODP Site U1406 (Figures 5u–5x and 7): the declination rotates by only ~90° and inclination does not decrease below ~0°. It is unclear whether this is a true geomagnetic feature or a coring or diagenetic artifact, so we refrain from assigning an age or duration to this feature.

The brief normal polarity interval in Subchron C6AAr.2r, previously identified at IODP Site U1334 (Channell et al., 2013), is not recorded at IODP Site U1406. Potential explanations for this observation include (1) a transient interval of low sedimentation rates at IODP Site U1406 during this geomagnetic event, (2) nonuniform geomagnetic field behavior during reversals (e.g., Glatzmaier & Roberts, 1995), or (3) poor preservation of the magnetic signal (e.g., Kodama, 2012). Despite generally high LSRs at IODP Site U1406, sedimentation rates in sediment drifts are commonly more variable than at pelagic sites (e.g., Rebesco et al., 2014). A transient interval with low LSR could have occurred in Subchron C6AAr.2r, and a low LSR reduces the possibility that short-duration geomagnetic features can be accurately reconstructed, due to lock-in and smoothing effects during the recording of the paleomagnetic signal (e.g., Roberts & Winklhofer, 2004).

Nonuniform geomagnetic field behavior during reversals can also influence the recording of a short-duration polarity event. Both magnetohydrodynamic models of reversals (e.g., Glatzmaier & Roberts, 1995) and paleointensity records of geomagnetic reversals preserved in flood basalts (e.g., Prévot et al., 1985) reveal that the axial dipole moment deteriorates to zero and then increases in strength in the opposite direction. During the weak dipole reversal phase, nondipole components may dominate and determine where and with what characteristics the magnetic field is recorded. The influence of such nondipole components varies with latitude, and may therefore have a different effect on equatorial sites, e.g., IODP Site U1334 (Channell et al., 2013), than on midlatitude sites, e.g., IODP Site U1406 studied here. It is important to note that it is currently uncertain if sediments are able to accurately record weak transitional directions, with arguments in favor of (e.g., Laj & Channell, 2015) and against (e.g., Valet et al., 2016) this hypothesis. A latitudinally dispersed stack of VGPs of the last four reversals (e.g., Clement, 2004) and numerical geodynamo models (Wicht, 2005; Wicht et al., 2009) also suggest that the duration of a polarity transition increases with the latitude at which the transition is observed or recorded. This means that equatorial records (e.g., ODP Site 1218 and IODP Site U1334) are more likely to record the discrete polarity boundaries and stable polarity phase of short-duration subchrons than midlatitude to high-latitude records (e.g., ODP Site 1090 and IODP Site U1406), assuming similar sedimentation rates at all sites. We also note that quasi-stable, transitional directions of short-duration polarity events identified at Site U1406 may be filtered out by our noise-reducing protocol. The noise-reducing protocol helps identifying well-expressed features in the magnetostratigraphic data, but it may not be suited to aid the identification of weakly expressed features such as transitional directions with weaker moments and outlier directions.

When evaluating the occurrence and fidelity of short-duration polarity events at Site U1406, we must also consider chemical processes potentially affecting the magnetic signal. NRM intensity (average $\sim10^{-4}$ to 10^{-5} A/m after 20 mT peak AF demagnetization) of Site U1406 sediments is about 1–2 orders of magnitude lower than those of ODP Sites 1090, 1218, and IODP Site U1334 sediments (average $\sim10^{-3}$ A/m after 20 mT peak AF demagnetization). The long-term, down-core increase in NRM intensity at IODP Site U1406 probably reflects sedimentary compaction and changes in magnetic concentration, which is also observed in the shipboard dry bulk density (Norris et al., 2014, Figure 24). Partial reductive dissolution of iron oxides is one explanation for the weak NRM intensities encountered at Site U1406, supported by the generally grey-green

sediment color that is characteristic of reduced sediments (e.g., Channell et al., 2013; Giosan et al., 2002; Roberts, 2015). Further evidence comes from the presence of Mn^{2+} but little Fe^{2+} in the pore waters (Norris et al., 2014) that are also characteristic of reduced environments (Canfield & Thamdrup, 2009; Roberts, 2015). Diagenetic sulfate reduction, however, is unlikely, because the concentration of pore water sulfate is similar to seawater values (Norris et al., 2014) and because the modest level of organic-matter burial (total organic carbon <0.5 wt %, Norris et al., 2014) limits the activity of sulfate-reducers in these sediments. Therefore, it is less likely that remanence-carrying iron sulfides could have formed. We argue that the supply and degradation of organic matter drives changes in redox potential that reduces some of the magnetite but does not progress to sulfate reduction allowing the authigenic formation of remanence-carrying iron sulfides.

5.2. Dynamic Behavior in Sediment Drifts

Three stratigraphic complexities are present in the Oligocene to lower Miocene sediments from IODP Site U1406. First, contorted bedding attributable to slumping distorts bedding in all three holes in the middle of the Chron C9n interval (Figures 2b and 8). Second, the stratigraphic sequence recovered at IODP Site U1406 shows large interhole variability in the interval of Chron C6Cn (latest Oligocene to earliest Miocene; Figures 6 and 8; van Peer et al., 2017). Third, the well-developed glauconite horizon identified in the three holes at ~34.5 m CCSF-M marks a ~2 Myr hiatus in the lower Miocene (Figures 2a and 8), estimated from the revised Base of *S. belemnos* (Table 2) and the C6Ar/C6AAn reversal (Table 1).

Based on the magnetostratigraphic age model, the three stratigraphic complexities correlate broadly to intervals characterized by the highest benthic $\delta^{18}O$ values observed in records from the equatorial Pacific (Pälike et al., 2006b), equatorial Atlantic (Pälike et al., 2006a), and South Atlantic Oceans (Billups et al., 2004; Liebrand et al., 2016, 2017; Figure 8). The slump in the middle of the Chron C9n interval (~27 Ma) coincides with the coldest phase of the Mid-Oligocene Glacial Interval (MOGI; Liebrand et al., 2017). It is also associated with a change in the package architecture of sediment drifts on the Newfoundland margin, indicated by seismic reflector H4 (Boyle et al., 2017). Reflector H4 is interpreted to mark the transition between an underlying seismically transparent unit and an overlying wavy, mounded seismic unit (Boyle et al., 2017). Due to the similarities in the depocenter of these units, Boyle et al. (2017) hypothesize that it is unlikely that the depth and pathway of deep-water circulation changed substantially across H4. Seismic reflector H4 may therefore represent a change in the flow volume of the bottom water mass over the Newfoundland margin.

The interval with large interhole variability (Chron C6Cn, ~23 Ma) and the well-developed glauconite horizon (Chron C6Ar, ~21 Ma) also coincide with cold phases near the OMT climate event and in the early Miocene, respectively. In contrast to the slump in Chron C9n, however, the large interhole variability and the glauconite horizon intervals do not coincide with well-defined seismic reflectors on the Newfoundland margin. Pronounced lateral variability over short length scales between the three holes around the OMT climate event suggests that deposition of the sediment drifts was more dynamic during the OMT climate event than before and after it. The glauconite horizon highlights a period of prolonged exposure at the seabed that we interpret as a period of nondeposition. We hypothesize that bottom water currents and sediment supply influence sediment drift settings in similar fashion as observed in the Quaternary (e.g., Stow et al., 2008). In this context, the stratigraphic complexities reflect a change in sediment supply and bottom water current strength, for example, their combined ability to erode or deposit sediment at IODP Site U1406. As in the Quaternary period, these processes are likely modulated by global climate. Future work on water mass and sediment provenance tracers may help unravel the complex combined effects of tectonic events (e.g., opening or closing of gateways) and long-term paleoclimatic trends on bottom water circulation in northwest Atlantic Ocean during the Oligocene to early Miocene.

6. Conclusions

A noise-detecting protocol implemented to cull noisy or erroneous paleomagnetic directions from large, continuous paleomagnetic data sets substantially improves the signal-to-noise ratio of the magnetostratigraphy in weakly magnetized sediments of IODP Site U1406 and is ready for integration with the UPmag software suite (Xuan & Channell, 2009). We correlate our shore-based u-channel sample magnetostratigraphy for IODP Site U1406 to Chrons C6Ar through C9n of the GPTS (~21–27 Ma; Hilgen et al., 2012; Vandenberghe et al., 2012) using shipboard and shore-based biostratigraphic datums. We identify short-duration geomagnetic events in Chrons C6Br, C7Ar, and C7r, and maybe in Subchron C8n.1n, of which three were previously

identified by Channell et al. (2003, 2013) and Lanci et al. (2005). Rock magnetic properties of the sediments suggest these events are not recording artifacts but are genuine features of the geomagnetic field.

Two hiatuses (each ~2 Myr long, occurring during Chron C6Ar and C9n, ~21 and ~27 Ma, respectively) punctuate an otherwise continuous sediment drift record at Site U1406. Additionally, the magnetostratigraphy dates substantial interhole variability at Site U1406 to the Oligocene-Miocene Transition climate event. This observation highlights the dynamic character of sediment drifts and that the construction of a robust splice and age model for such depositional environments requires the integration of multiple independent stratigraphic data sets. The three intervals of stratigraphic complexity at Site U1406 broadly correspond to global cold periods inferred from correlation to benthic δ^{18}O records from ODP Sites 926, 1090, 1218, and 1264. We hypothesize that this stratigraphic complexity is caused by a change in sediment supply or bottom water current strength during colder climates. Future work on sediment and water mass provenance and their links to global climate may help test and refine our understanding of pre-Pliocene ocean circulation in the North Atlantic Ocean.

References

Acton, G. D. (2011). Zplotit. Retrieved from http://paleomag.ucdavis.edu/software-Zplotit.html

Acton, G. D., Okada, M., Clement, B. M., Lund, S. P., & Williams, T. (2002). Paleomagnetic overprints in ocean sediment cores and their relationship to shear deformation caused by piston coring. *Journal of Geophysical Research*, *107*(B4), 2067. https://doi.org/10.1029/2001JB000518

Berens, P. (2009). CircStat: A MATLAB toolbox for circular statistics. *Journal of Statistical Software*, *31*(10), 1–21. https://doi.org/10.18637/jss.v031.i10

Billups, K., Pälike, H., Channell, J. E. T., Zachos, J. C., & Shackleton, N. J. (2004). Astronomic calibration of the late Oligocene through early Miocene geomagnetic polarity time scale. *Earth and Planetary Science Letters*, *224*(1–2), 33–44. https://doi.org/10.1016/j.epsl.2004.05.004

Blakely, R. J. (1974). Geomagnetic reversals and crustal spreading rates during the Miocene. *Journal of Geophysical Research*, *79*(20), 2979–2985. https://doi.org/10.1029/JB079i020p02979

Bowles, J. (2007). Coring-related deformation of Leg 208 sediments from Walvis Ridge: Implications for paleomagnetic data. *Physics of the Earth and Planetary Interiors*, *161*(3–4), 161–169. https://doi.org/10.1016/j.pepi.2007.01.010

Boyle, P. R., Romans, B. W., Tucholke, B. E., Norris, R. D., Swift, S. A., & Sexton, P. F. (2017). Cenozoic North Atlantic deep circulation history recorded in contourite drifts, offshore Newfoundland, Canada. *Marine Geology*, *385*, 185–203. https://doi.org/10.1016/j.margeo.2016.12.014

Cande, S. C., & Kent, D. V. (1992). A new geomagnetic polarity time scale for the Late Cretaceous and Cenozoic. *Journal of Geophysical Research*, *97*(B10), 13917–13951. https://doi.org/10.1029/92JB01202

Cande, S. C., & Kent, D. V. (1995). Revised calibration of the geomagnetic polarity timescale for the Late Cretaceous and Cenozoic. *Journal of Geophysical Research*, *100*(B4), 6093–6095.

Cande, S. C., & LaBrecque, J. L. (1974). Behaviour of the Earth's palaeomagnetic field from small scale marine magnetic anomalies. *Nature*, *247*, 26–28.

Canfield, D. E., & Thamdrup, B. (2009). Towards a consistent classification scheme for geochemical environments, or, why we wish the term "suboxic" would go away. *Geobiology*, *7*(4), 385–392. https://doi.org/10.1111/j.1472-4669.2009.00214.x

Channell, J. E. T., Galeotti, S., Martin, E. E., Billups, K., Scher, H. D., & Stoner, J. S. (2003). Eocene to Miocene magnetostratigraphy, biostratigraphy, and chemostratigraphy at ODP Site 1090 (sub-Antarctic South Atlantic). *Geological Society of America Bulletin*, *115*(5), 607–623. https://doi.org/10.1130/0016-7606(2003)115<0607:ETMMBA>2.0.CO;2

Channell, J. E. T., Ohneiser, C., Yamamoto, Y., & Kesler, M. S. (2013). Oligocene-Miocene magnetic stratigraphy carried by biogenic magnetite at sites U1334 and U1335 (equatorial Pacific Ocean). *Geochemistry, Geophysics, Geosystems*, *14*, 265–282. https://doi.org/10.1029/2012GC004429

Clement, B. M. (2004). Dependence of the duration of geomagnetic polarity reversals on site latitude. *Nature*, *428*(6983), 637–640. https://doi.org/10.1038/nature02459

Dunlop, D. J., & Özdemir, Ö. (2007). Magnetizations in rocks and minerals. In G. Schubert (Ed.), *Treatise on geophysics* (Vol. 5, pp. 277–336). Oxford, UK: Elsevier. https://doi.org/10.1016/B978-044452748-6.00093-6

Egli, R. (2013). VARIFORC: An optimized protocol for calculating non-regular first-order reversal curve (FORC) diagrams. *Global and Planetary Change*, *110*, 302–320. https://doi.org/10.1016/j.gloplacha.2013.08.003

Egli, R., Chen, A. P., Winklhofer, M., Kodama, K. P., & Horng, C.-S. (2010). Detection of noninteracting single domain particles using first-order reversal curve diagrams. *Geochemistry, Geophysics, Geosystems*, *11*, Q01Z11. https://doi.org/10.1029/2009GC002916

Giosan, L., Flood, R. D., Gru, J., & Mudie, P. (2002). Paleoceanographic significance of sediment color on western North Atlantic Drifts: II. Late Pliocene-Pleistocene sedimentation. *Marine Geology*, *189*, 43–61.

Glatzmaier, G. A., & Roberts, P. H. (1995). A three-dimensional self-consistent computer simulation of a geomagnetic field reversal. *Nature*, *377*(6546), 203–209. https://doi.org/10.1038/377203a0

Harrison, R. J., & Feinberg, J. M. (2008). FORCinel: An improved algorithm for calculating first-order reversal curve distributions using locally weighted regression smoothing. *Geochemistry, Geophysics, Geosystems*, *9*, Q05016. https://doi.org/10.1029/2008GC001987

Heslop, D., & Roberts, A. P. (2012). Estimation of significance levels and confidence intervals for first-order reversal curve distributions. *Geochemistry, Geophysics, Geosystems*, *13*, Q12Z40. https://doi.org/10.1029/2012GC004115

Heslop, D., & Roberts, A. P. (2016). Analyzing paleomagnetic data: To anchor or not to anchor? *Journal of Geophysical Research: Solid Earth*, *121*, 1–12. https://doi.org/10.1002/2016JB013387

Hilgen, F. J., Lourens, L. J., & Van Dam, J. A. (2012). The Neogene period. In F. M. Gradstein, J. G. Ogg, M. D. Schmitz, & G. M. Ogg (Eds.), *The geological time scale* (pp. 923–978). Amsterdam, the Netherlands: Elsevier B.V.

Jackson, M., & Solheid, P. (2010). On the quantitative analysis and evaluation of magnetic hysteresis data. *Geochemistry, Geophysics, Geosystems*, *11*, Q04Z15. https://doi.org/10.1029/2009GC002932

Kirschvink, J. L. (1980). The least-squares line and plane and the analysis of palaeomagnetic data. *Geophysical Journal of the Royal Astronomical Society*, *62*(3), 699–718.

Kodama, K. (2012). *Paleomagnetism of sedimentary rocks: Process and interpretation*. Chichester, UK: Wiley-Blackwell.

LaBrecque, J. L., Kent, D. V., & Cande, S. C. (1977). Revised magnetic polarity timescale for the Late Cretaceous and Cenozoic time. *Geology*, *5*, 330–335. https://doi.org/10.1130/0091-7613(1977)5<330:RMPTSF>2.0.CO;2

Laj, C., & Channell, J. E. T. (2015). Geomagnetic excursions. In G. Schubert (Ed.), *Treatise on geophysics* (2nd ed., Vol. 5, pp. 373–416). Oxford, UK: Elsevier B.V. https://doi.org/10.1016/B978-044452748-6.00095-X

Lanci, L., Parés, J. M., Channell, J. E. T., & Kent, D. V. (2005). Oligocene magnetostratigraphy from Equatorial Pacific sediments (ODP Sites 1218 and 1219, Leg 199). *Earth and Planetary Science Letters*, *237*(3–4), 617–634. https://doi.org/10.1016/j.epsl.2005.07.004

Li, J., Wu, W., Liu, Q., & Pan, Y. (2012). Magnetic anisotropy, magnetostatic interactions and identification of magnetofossils. *Geochemistry, Geophysics, Geosystems*, *13*, Q10Z51. https://doi.org/10.1029/2012GC004384

Liebrand, D., Beddow, H. M., Lourens, L. J., Pälike, H., Raffi, I., Bohaty, S. M., . . . Batenburg, S. J. (2016). Cyclostratigraphy and eccentricity tuning of the early Oligocene through early Miocene (30.1–17.1 Ma): *Cibicides mundulus* stable oxygen and carbon isotope records from Walvis Ridge Site 1264. *Earth and Planetary Science Letters*, *450*, 392–405. https://doi.org/10.1016/j.epsl.2016.06.007

Liebrand, D., de Bakker, A. T. M., Beddow, H. M., Wilson, P. A., Bohaty, S. M., Ruessink, G., . . . Lourens, L. J. (2017). Evolution of the early Antarctic ice ages. *Proceedings of the National Academy of Sciences of the United States of America*, *114*(15), 3867–3872. https://doi.org/10.1073/pnas.1615440114

Norris, R. D., Wilson, P. A., Blum, P., Fehr, A., Agnini, C., Bornemann, A., . . . Yamamoto, Y. (2014). Site U1406. In R. D. Norris et al. (Eds.), *Proceedings of the Integrated Ocean Drilling Program* (Vol. 342). College Station, TX: Integrated Ocean Drilling Program. https://doi.org/10.2204/iodp.proc.342.107.2014

Oda, H., & Xuan, C. (2014). Deconvolution of continuous paleomagnetic data from pass-through magnetometer: A new algorithm to restore geomagnetic and environmental information based on realistic optimization. *Geochemistry, Geophysics, Geosystems*, *15*, 1–18. https://doi.org/10.1002/2014GC005513

Pälike, H., Frazier, J., & Zachos, J. C. (2006a). Extended orbitally forced palaeoclimatic records from the equatorial Atlantic Ceara Rise. *Quaternary Science Reviews*, *25*(23–24), 3138–3149. https://doi.org/10.1016/j.quascirev.2006.02.011

Pälike, H., Norris, R. D., Herrle, J. O., Wilson, P. A., Coxall, H. K., Lear, C. H., . . . Wade, B. S. (2006b). The Heartbeat of the Oligocene climate system. *Science*, *314*(5807), 1894–1898. https://doi.org/10.1126/science.1133822

Pike, C. R., Roberts, A. P., & Verosub, K. L. (1999). Characterizing interactions in fine magnetic particle systems using first order reversal curves. *Journal of Applied Physics*, *85*(9), 6660–6667.

Prévot, M., Mankinen, E. A., Coe, R. S., & Grommé, C. S. (1985). The Steens Mountain (Oregon) geomagnetic polarity transition: 2. Field intensity variations and discussion of reversal models. *Journal of Geophysical Research*, *90*(B12), 10417–10448. https://doi.org/10.1029/JB090iB12p10417

Rebesco, M., Hernández-Molina, F. J., Van Rooij, D., & Wåhlin, A. (2014). Contourites and associated sediments controlled by deep-water circulation processes: State-of-the-art and future considerations. *Marine Geology*, *352*, 111–154. https://doi.org/10.1016/j.margeo.2014.03.011

Roberts, A. P. (2015). Magnetic mineral diagenesis. *Earth Science Reviews*, *151*, 1–47. https://doi.org/10.1016/j.earscirev.2015.09.010

Roberts, A. P., Chang, L., Heslop, D., Florindo, F., & Larrasoana, J. C. (2012). Searching for single domain magnetite in the "pseudo-single-domain" sedimentary haystack: Implications of biogenic magnetite preservation for sediment magnetism and relative paleointensity determinations. *Journal of Geophysical Research*, *117*, 1–26. https://doi.org/10.1029/2012JB009412

Roberts, A. P., Florindo, F., Chang, L., Heslop, D., Jovane, L., & Larrasoaña, J. C. (2013). Magnetic properties of pelagic marine carbonates. *Earth Science Reviews*, *127*, 111–139. https://doi.org/10.1016/j.earscirev.2013.09.009

Roberts, A. P., Heslop, D., Zhao, X., & Pike, C. R. (2014). Understanding fine magnetic particle systems through use of first-order reversal curve diagrams. *Reviews of Geophysics*, *52*, 557–602. https://doi.org/10.1002/2014RG000462

Roberts, A. P., Pike, R., & Verosub, K. L. (2000). First-order reversal curve diagrams: A new tool for characterizing the magnetic properties of natural samples. *Journal of Geophysical Research*, *105*(B12), 28461–28475. https://doi.org/10.1029/2000JB900326

Roberts, A. P., & Winklhofer, M. (2004). Why are geomagnetic excursions not always recorded in sediments? Constraints from post-depositional remanent magnetization lock-in modelling. *Earth and Planetary Science Letters*, *227*(3–4), 345–359. https://doi.org/10.1016/j.epsl.2004.07.040

Stow, D. A. V., Hunter, S., Wilkinson, D., & Hernández-Molina, F. J. (2008). The nature of contourite deposition. In M. Rebesco & A. Camerlenghi (Eds.), *Developments in sedimentology* (Vol. 60, pp. 143–156). Amsterdam, the Netherlands: Elsevier B.V. https://doi.org/10.1016/S0070-4571(08)10009-7

Tauxe, L., LaBrecque, J. L., Dodson, R., Fuller, M., & DeMatteo, J. (1983). U-channels - A new technique for paleomagnetic analysis of hydraulic piston cores. *Eos, Transactions American Geophysical Union*, *64*, 219.

Valet, J.-P., Meynadier, L., Simon, Q., & Thouveny, N. (2016). When and why sediments fail to record the geomagnetic field during polarity reversals. *Earth and Planetary Science Letters*, *453*, 96–107. https://doi.org/10.1016/j.epsl.2016.07.055

Vandamme, D. (1994). A new method to determine paleosecular variation. *Physics of the Earth and Planetary Interiors*, *85*(1–2), 131–142. https://doi.org/10.1016/0031-9201(94)90012-4

Vandenberghe, N., Hilgen, F. J., & Speijer, R. P. (2012). The Paleogene period. In F. M. Gradstein, J. G. Ogg, M. Schmitz, & G. Ogg (Eds.), *A geological time scale* (pp. 855–921). Amsterdam, the Netherlands: Elsevier B.V. https://doi.org/10.1016/B978-0-444-59425-9.00028-7

van Hinsbergen, D. J. J., de Groot, L. V., van Schaik, S. J., Spakman, W., Bijl, P. K., Sluijs, A., . . . Brinkhuis, H. (2015). A paleolatitude calculator for paleoclimate studies. *PloS ONE*, *10*(6), e0126946. https://doi.org/10.1371/journal.pone.0126946

van Peer, T. E., Liebrand, D., Xuan, C., Lippert, P. C., Agnini, C., Blum, N., . . . Wilson, P. A. (2017). Data report: Revised composite depth scale and splice for IODP Site U1406. In R. D. Norris, P. A. Wilson, P. Blum, & Scientists Expedition 342 (Eds.), *Proceedings of the Integrated Ocean Drilling Program* (Vol. 342, pp. 1–23). College Station, TX: Integrated Ocean Drilling Program. https://doi.org/10.2204/iodp.proc.342.202.2017

Weeks, R., Laj, C., Endignoux, L., Fuller, M., Roberts, A., Manganne, R., . . . Goree, W. (1993). Improvements in long-core measurement techniques: Applications in palaeomagnetism and palaeoceanography. *Geophysical Journal International*, *114*, 651–662.

Wicht, J. (2005). Palaeomagnetic interpretation of dynamo simulations. *Geophysical Journal International*, *162*(2), 371–380. https://doi.org/10.1111/j.1365-246X.2005.02665.x

Wicht, J., Stellmach, S., & Harder, H. (2009). Numerical models of the geodynamo: From fundamental Cartesian models to 3d simulations of field reversals. In K.-H. Glassmeier, H. Soffel, & J. F. W. Negendank (Eds.), *Geomagnetic field variations* (pp. 114–165). Berlin, Germany: Springer.

Xuan, C., & Channell, J. E. T. (2009). UPmag: MATLAB software for viewing and processing u channel or other pass-through paleomagnetic data. *Geochemistry, Geophysics, Geosystems*, *10*, Q10Y07. https://doi.org/10.1029/2009GC002584